

1 **Cohesive and mixed sediment in the Regional Ocean Modeling**
2 **System (ROMS v3.6) implemented in the Coupled Ocean**
3 **Atmosphere Wave Sediment-Transport Modeling System**
4 **(COAWST r1179)**

5 Christopher R. Sherwood¹, Alfredo L. Aretxabaleta¹, Courtney K. Harris², J. Paul Rinehimer^{2,3},
6 Romaric Verney⁴, Bénédicte Ferré^{1,5}

7 ¹U. S. Geological Survey, 384 Woods Hole Road, Woods Hole, MA 02543-1598 USA

8 ²Virginia Institute of Marine Sciences, Gloucester Point, Virginia, USA

9 ³Currently at WEST Consultants, Bellevue, WA, USA

10 ⁴IFREMER, Plouzane, France

11 ⁵Currently at CAGE-Centre for Arctic Gas Hydrate, Environment, and Climate; Department of Geosciences, UiT The Arctic
12 University of Norway, N-9037 Tromsø, Norway

13

14 *Correspondence to:* Christopher R. Sherwood (csherwood@usgs.gov)

15 **Abstract.** We describe and demonstrate algorithms for treating cohesive and mixed sediment that have been added to the
16 Regional Ocean Modeling System (ROMS version 3.6), as implemented in the Coupled Ocean Atmosphere Wave Sediment-
17 Transport Modeling System (COAWST Subversion repository revision 1179). These include: flocculation dynamics (aggregation
18 and disaggregation in the water column); changes in flocculation characteristics in the seabed; erosion and deposition of cohesive
19 and mixed (combination of cohesive and non-cohesive) sediment; and bioturbative mixing of bed sediment. These routines
20 supplement existing non-cohesive sediment modules, thereby increasing our ability to model fine-grained and mixed-
21 sediment environments. Additionally, we describe changes to the sediment bed-layering scheme that improve the fidelity of
22 the modeled stratigraphic record. Finally, we provide examples of these modules implemented in idealized test cases and a
23 realistic application.

24

25 **Copyright statement**

26 The authors' copyright for this publication is transferred to the U.S. Government.

27 **1 Introduction**

28 **1.1 Motivation**

29 Fine cohesive sediment (mud) is present in almost every coastal environment, and influences water clarity, benthic habitats,
30 shoaling of harbors and channels, storage and transport of nutrients and contaminants, and morphologic evolution of
31 wetlands, deltas, estuaries, and muddy continental shelves (Winterwerp and van Kesteren, 2004; Edmonds and Slingerland,
32 2010; Caldwell and Edmonds, 2014; Mehta, 2014; Li et al., 2017). The properties and behavior of mud depend on more than
33 the size, shape, and density of the individual particles, so they are more difficult to characterize and model than properties of
34 non-cohesive material like sand. Cohesive sediment often forms flocs that have lower densities, larger diameters, and faster
35 settling velocities than the primary particles. Acoustic and optical sensors respond differently to suspensions of flocculated
36 sediment, compared with similar mass concentrations of unflocculated particles, and these responses have important
37 influences on observations of suspended-sediment mass concentrations, especially in estuaries (for example, McCave and
38 Swift, 1976; McCave, 1984; Eisma, 1986; Hill and Nowell, 1995; Winterwerp, 1999, 2002; Winterwerp et al., 2006; Xu,
39 Wang, and Riemer, 2008; 2010; Verney et al., 2011; Slade, Boss, and Russo, 2011; MacDonald et al., 2013; Thorne et al.,
40 2014).

41 Cohesive sediment beds are distinguished by generally finer sediment, including some clay content, often are poorly sorted,
42 and have low bulk density (high water content). Cohesive beds have a tendency for bulk responses to bottom stress, rather
43 than individual particle responses. Cohesive beds have rheological properties that can range from fluids to Bingham plastics
44 to granular materials, and may change with time in response to changes in water content, biochemical processes and fluid or
45 geomechanical stresses (Dyer, 1986; Whitehouse et al., 2000; Winterwerp and Kranenburg, 2002; Winterwerp and van
46 Kesteren, 2004; Maa et al., 2007; Knoch and Malcherek, 2011; Mehta, 2014).

47 Sediment transport in coastal ocean models is sensitive to the representation of fine-scale stratigraphy because evolving
48 seabed properties determine what sediment is exposed to the water column and available for transport. Small-scale
49 stratigraphy and grain-size distribution at the sediment-water interface also influence the grain roughness of the seabed,
50 affect the type of small-scale roughness (biogenic features and ripples) present on the bed, and control properties like
51 acoustic impedance of the seafloor. Biodiffusion influences stratigraphy by reducing gradients in grain size and other bed
52 properties and by mixing materials from deeper in the bed to closer to the surface, where they may be more susceptible to
53 transport.

54 1.2 Previous Modeling Efforts

55 Amoudry and Souza (2011) surveyed regional-scale sediment-transport and morphology models, and found that one of the
56 shortcomings was the treatment of cohesive- and mixed-sediment models. The water-column behavior of cohesive sediment
57 (e.g., flocculation and disaggregation, and settling) and the consolidation of settling particles to form a cohesive bed has been
58 modeled mostly with one-dimensional vertical (1DV) models or with empirical formulae that allow particle settling velocity
59 to vary as a function of salinity (Ralston et al., 2012) or suspended-sediment concentration (e.g., Mehta, 1986; Lick et al.,
60 1993; Van Leussen, 1994; Lumborg and Windelin, 2003; Lumborg, 2005; and Lumborg and Pejrup, 2005). Mietta et al.
61 (2009) have demonstrated the effect that pH and organic-matter content have on mean floc size and settling velocity. The
62 primary dynamical effect of flocculation is to increase settling velocities, thereby increasing the mass settling flux. Soulsby
63 et al. (2013) reviewed methods for estimating floc settling velocities and proposed a new formulation that depends primarily
64 on turbulence shear and instantaneous suspended-sediment concentration. Spearman et al. (2011) noted that adjustments to
65 settling velocity (e.g., Manning and Dyer, 2007) were able to successfully reproduce floc settling in one-dimensional estuary
66 modeling applications. However, approaches that adjust only settling velocity do not allow analysis of other characteristics
67 of the suspended particle field, such as particle size and density, which affect acoustic and optical properties, or geochemical
68 properties (water content and surface area). Full floc dynamics have been incorporated in only a few coastal hydrodynamics
69 and sediment-transport models. Winterwerp (2002) incorporated his floc model (Winterwerp, 1999) in a three-dimensional
70 simulation of the estuary turbidity maximum (ETM) in the Ems estuary. Ditschke and Markofsky (2008) described
71 formulations in TELEMAC-3D to represent exchanges among size classes from floc dynamics. Xu et al. (2010) added floc
72 dynamics to the Princeton Ocean Model (POM) and simulated the ETM in Chesapeake Bay. Empirical formulae for the
73 erosion of cohesive sediment have been derived from laboratory flume measurements and field experiments (Whitehouse et
74 al, 2000; Mehta, 2014). Many have a form similar to the Ariathurai and Arulanandan (1978) equation used in ROMS
75 (Warner et al., 2008), which relates erosional flux E ($\text{kg m}^{-2} \text{s}^{-1}$) to the normalized excess shear stress as
76 $E = E_0(1 - \phi) [(\tau_{sf} - \tau_c) / \tau_{sf}]$ when $\tau_{sf} > \tau_c$, and where E_0 ($\text{kg m}^{-2} \text{s}^{-1}$) is an empirical rate constant, ϕ (m^3/m^3) is sediment
77 porosity, τ_{sf} (Pa) is the skin-friction component of the bottom shear stress, and τ_c (Pa) is the critical shear stress for erosion.
78 Erosion of cohesive sediment in some models (for example Delft3D; van der Wegen et al., 2011; Caldwell and Edmonds,
79 2014) uses a similar formulation, subject to a user-specified critical shear stress for erosion. It is recognized that τ_c may
80 increase with depth in sediment, and erosion-rate formulae have been proposed that incorporate depth-dependent profiles for
81 E_0 and/or τ_c (Whitehouse et al, 2000; Mehta, 2014). Wiberg et al. (1994) demonstrated the need to account for small-scale
82 stratigraphy to represent bed armoring for a non-cohesive model, and did so via a layered bed model that kept track of
83 changes to sediment-bed grain-size distribution in response to cycles of erosion and deposition. Bed layers have been used to

84 represent temporal changes to bed erodibility for fine-grained sediment, for example by using an age model for the bed
85 (HydroQual, 2004). Biodiffusion may alter stratigraphy, and there are many 1DV models that treat diffusive mass flux of
86 sediment and reactive constituents in the bed, mostly motivated by water-quality and geochemical concerns (e.g., Boudreau,
87 1997; DiToro, 2001; Winterwerp and van Kesteren, 2004). Several regional-scale circulation and sediment-transport models
88 treat sediment stratigraphy, including ECOMSED (HydroQual, 2004), ROMS/CSTMS (Warner et al., 2008), Delft3D (van
89 der Wegen et al., 2011), FVCOM, TELEMAC/SISYPHE (Villaret et al., 2007; Tassi and Villaret, 2014), MARS3D (Le Hir,
90 2011; Mengual et al., 2017) and some have unpublished treatments for cohesive processes. Sanford (2008) pioneered an
91 approach where the critical shear stress for each bed layer was nudged toward an assumed equilibrium value, and the critical
92 stress for erosion of the surface layer alternately became smaller or larger in response to deposition and erosion. We have
93 combined the approach of Sanford et al. (2008) with biodiffusive mixing to represent depth-dependent changes in erodibility.
94 This approach has been implemented in the cohesive bed stratigraphy algorithm in ROMS (described here) and applied by
95 Rinehimer et al. (2008), Butman et al. (2014), and Fall et al. (2014).

96 **1.3 Goals of the Model**

97 Our goal in developing and refining sediment dynamics in ROMS is to produce an open-source community model
98 framework useful for research and management that combines cohesive and non-cohesive behavior and is suitable for
99 simulating sediment transport, stratigraphic evolution, and morphologic change. Our goal is to develop methods that can be
100 implemented within coastal and estuarine models for application at regional scales, i.e. domains of 10s to 100s of km² with
101 grid elements of 10 – 10,000 m² and the ability to resolve time scales ranging from minutes to decades.

102 **1.4 Objectives and Outline of the Paper**

103 The behavior of non-cohesive sediment (sand) in ROMS was described by Warner et al. (2008). ROMS also includes several
104 biogeochemical modules (Fasham et al., 1990; Fennel et al., 2006). New components have since been added, including
105 spectral irradiance and seagrass growth models (del Barrio et al., 2014) and a model for treating the effects of submerged
106 aquatic vegetation on waves and currents (Beudin et al., 2017). The present paper describes new components that model
107 processes associated with cohesive sediment (mud) and mixtures of sand and mud. These include aggregation and
108 disaggregation of flocs in the water column, sediment exchange with a cohesive bed where erosion is limited by a bulk
109 critical shear stress parameter that increases with burial depth, and tracking stratigraphic changes in response to deposition,
110 erosion, and biodiffusive mixing. Our goal is to demonstrate that the algorithms reproduce some of the important behaviors
111 that distinguish cohesive sedimentary environments from sandy ones, and to demonstrate their utility for modeling muddy
112 environments. The model processes are presented and discussed in Section 2. Additional details of the model implementation

113 and their use in ROMS are presented in the Supplement. Examples of model behavior are presented in Section 3, and a
114 realistic application in the York River Estuary is presented in Section 4. Discussion and Conclusions are in Sections 5 and 6.

115 **2 Model Processes**

116 Flocculation is represented as a local process of aggregation and disaggregation that moves mass among the flocculation
117 within each model grid cell during a ROMS baroclinic time step. ROMS uses a split time step scheme that integrates over
118 several (ca. 20) depth-averaged (barotropic) time steps before the depth-dependent baroclinic equations are integrated
119 (Shchepetkin and McWilliams, 2005). Subsequent advection and mixing of flocculation particles is performed along with other
120 tracers (heat, salt, sand, biogeochemical constituents). The water column is coupled with the sediment bed via depositional
121 fluxes determined by near-bed concentrations, settling velocities, and threshold shear stresses; and via erosional fluxes
122 determined by bottom shear stresses, bulk and particle critical shear stresses for erosion, and sediment availability in the top,
123 active layer (Warner et al., 2008). The distribution of mass among the cohesive classes can change in the bed as flocculation
124 converted to denser aggregates. Deposition and erosion affect the mass of sediment classes in the stratigraphic record, which
125 can also be changed by bioturbation mixing and a heuristic model of erodibility as a function of time and sediment depth.
126 Each of these processes is described below.

127 **2.1 Properties of Sediment, Seafloor, and Seabed**

128 ROMS accounts for two distinct types of sediment: non-cohesive sediment (e.g., sand) and cohesive sediment (e.g., mud).
129 The general framework used to represent sediment and the seabed is unchanged from Warner et al. (2008), except that the
130 expanded model requires additional variables to allow for both cohesive and non-cohesive classes. The number of sediment
131 classes is presently limited to twenty-two of each type by the input/output formats, but is otherwise only constrained by
132 computational resources. Each class must be classified as either non-cohesive or cohesive, and at least one class of one type
133 is required for sediment-transport modeling. Each class is associated with properties (diameter, density, critical shear stresses
134 for erosion and deposition, settling velocity) that are specified as input and remain constant throughout the model
135 calculations. Seafloor properties that describe the condition of the sediment surface are stored with spatial dimensions that
136 correspond to the horizontal model domain. Seafloor properties include representative values (geometric means) of sediment
137 properties in the top layer, including grain size, critical shear stress for erosion, settling velocity, and density; and properties
138 of the sediment surface, such as ripple height, ripple wavelength, and bottom roughness. Seabed properties (i.e. stratigraphy)
139 are tracked at each horizontal location and in each layer in the bed. The number of layers used to represent seabed properties
140 is specified as input and remains constant throughout the model run. The mass of each sediment class, bulk porosity, and
141 average sediment age is stored for each bed layer. The layer thickness, which is calculated from porosity and the mass and

142 sediment density for each class is stored for convenience, as is the depth to the bottom of each layer. Additional information
143 for bulk critical shear stress is stored if the cohesive sediment formulation is being used.

144 **2.2 Floc Model**

145 Maerz et al. (2011) note that there are two approaches for representing particle sizes in models. Distribution-based models
146 use one value (e.g., the average or median) to represent the particle size distribution and sometimes floc density.
147 Distribution-based models are the most common: examples include Winterwerp (2006), Manning and Dyer (2007), and
148 Khelifa and Hill (2006). Van Leussen (1998) and Soulsby et al. (2013) provide reviews. In a numerical model, distribution-
149 based models require advection schemes that allow for spatial and temporal variation of settling velocity. In contrast, size-
150 class-based models represent the particle population by apportioning mass among a discrete number of size classes through
151 semi-empirical descriptions of break-up and aggregation, following the pioneering work of Smoluchowski (1917). Recent
152 examples include Hill and Nowell (1995), Xu et al. (2008), and Verney et al. (2011). One advantage of class-based models is
153 that simpler and more efficient advection schemes designed for constant settling velocities can be used for each class in turn.
154 The tradeoff is that (many) more size classes are required. Our implementation takes the second approach, and we
155 characterize sediment and floc distributions with several (7 – 20+) classes, each with fixed characteristics including size, floc
156 density, and settling velocity. This allows us to take advantage of the efficient settling flux algorithms in ROMS.

157 **2.2.1. Water-Column Processes**

158 We implemented the floc model FLOCMOD (Verney et al., 2011) in ROMS to model changes in settling velocity and
159 particle size caused by aggregation and disaggregation. The floc model is a zero-dimensional model that is locally integrated
160 over the baroclinic time step, from initial to final conditions, in every cell of the ROMS model. After the floc populations are
161 updated, the normal settling, advection, and diffusion routines used for tracers (heat, salt, flocs or other sediment,
162 biogeochemical constituents) in ROMS are advanced, with flux boundary conditions at the bed (erosion or deposition) and
163 zero-flux conditions at the surface. FLOCMOD is a population model (Smoluchowski, 1917) based on a finite number of
164 size classes with representative floc diameters D_f (m). The model requires a relationship between floc size and floc density
165 ρ_f (kg/m³) that is related to the primary disaggregated particle diameter D_p (m) and density ρ_s (kg/m³) through a fractal
166 dimension n_f (dimensionless; Kranenburg, 1994) according to

$$167 \quad \rho_f = \rho_w + (\rho_s - \rho_w) \left(\frac{D_f}{D_p} \right)^{n_f - 3} \quad (1)$$

168 where ρ_w (kg/m³) is the density of the interstitial water in the flocs. The fractal dimension for natural flocs is typically close
 169 to 2.1 (Tambo and Watanabe, 1979; Kranenburg, 1994). Floc densities increase as n_f increases, and at $n_f = 3$, the flocs are
 170 solid particles with $\rho_f = \rho_s$. All cohesive sediment classes are treated as flocs when the floc model is invoked, and the
 171 processes of aggregation and disaggregation can shift mass of suspended sediment from one class to another. The floc model
 172 is formulated as a Lagrangian process that takes place within a model cell over a baroclinic model time step while
 173 conserving suspended mass in that cell, similar to the way that reaction terms are included in biogeochemical models (for
 174 example, Fennel et al., 2006). FLOCMOD simulates aggregation from two-particle collisions caused by either shear or
 175 differential settling, and disaggregation caused by turbulence shear and/or collisions. The rate of change in the number
 176 concentration $N(k)$ (m⁻³) of particles in the k^{th} floc class is controlled by a coupled set of k of differential equations

$$177 \quad \frac{dN(k)}{dt} = G_a(k) + G_{bs}(k) + G_{bc}(k) - L_a(k) - L_{bs}(k) - L_{bc}(k) \quad (2)$$

178 where G and L terms (m⁻³s⁻¹) represent gain and loss of mass by the three processes denoted by subscripts: a (aggregation),
 179 bs (breakup caused by shear), and bc (breakup caused by collisions). Equations 2 are integrated explicitly using adjustable
 180 time steps that may be as long as the baroclinic model time step, but are decreased automatically when necessary to ensure
 181 stability and maintain positive particle number concentrations. Particle number concentrations $N(k)$ are related to suspended
 182 mass concentrations $C_m(k)$ (kg/m³) via the volume and density of individual flocs. The aggregation and disaggregation terms
 183 (Verney et al., 2011) both depend on local rates of turbulence shear, which are calculated from the turbulence submodel in
 184 ROMS. Details of these processes are described in the Supplement.

185 The floc model introduces several parameters (see Supplement), some of which have been evaluated by Verney et al. (2011).
 186 These parameters are specified by the user. The equilibrium floc size depends on the ratio of aggregation to breakup
 187 parameters, and the rate of floc formation and destruction depends on their magnitudes (Winterwerp, 1999; 2002). The
 188 diameter, settling velocity, density, critical stress for erosion, and critical stress for deposition (described below) are required
 189 inputs for each sediment class, both cohesive and non-cohesive (see Supplement). The present implementation requires a
 190 fractal relationship between floc diameter and floc density (Kranenburg, 1994), and we have assumed a Stokes settling
 191 velocity. Alternative relationships between diameter and settling velocity, such as modified Stokes formula (e.g.,
 192 Winterwerp, 2002; Winterwerp et al., 2002; Winterwerp et al., 2007; Droppo et al., 2005; Khelifa and Hill, 2006), could be
 193 used by adjusting input parameters, but alternative relationships between diameter and floc density (Khelifa and Hill, 2006;
 194 Nguyen and Chua, 2011) would require changes to the aggregation and disaggregation terms in FLOCMOD.

195 2.2.3. Changes in floc size distribution within the bed

196 Changes in the size-class distribution of flocs are expected once they have been incorporated into the seabed, in contrast to
197 non-cohesive particles that retain their properties during cycles of erosion and deposition. For example, it seems unlikely that
198 large, low-density flocs can be buried and later resuspended intact, and limited published observations suggest that material
199 deposited as flocs can be eroded as denser, more angular aggregates (Stone et al., 2008). However, we find little guidance for
200 constraining this process. We therefore have implemented floc evolution in the bed, a simple process that stipulates an
201 equilibrium cohesive size-class distribution and an associated relaxation time scale. The time-varying size-class distribution
202 in the bed tends toward the user-specified equilibrium distribution while conserving mass (see Supplement). If the
203 equilibrium distribution includes more smaller, denser particles and less larger, less-dense particles than the depositing flocs,
204 the particle population in the bed will evolve toward smaller, denser particles, changing the amount of material in the classes
205 that are available for resuspension when a cohesive bed is eroded. Example cases presented below demonstrate the effect of
206 this process and the associated time scale on floc distributions both in the bed and in the water column.

207 2.3. Bed – Water-Column Exchange

208 2.2.1. Fluxes into the bed – Critical shear stress for deposition

209 The settling flux of flocs (and all other size classes) into the bed (deposition) over a time step is calculated as $w_{s,k} \rho_k C_{v,k} \Delta t$
210 (kg m^{-2} , where $w_{s,k}$ (m/s), ρ_k (kg/m^3), and $C_{v,k}$ (m^3/m^3) are settling velocities, floc (or particle) densities, and volume
211 concentrations for the k th size class in the bottom-most water-column layer, respectively, and Δt (s) is the baroclinic time
212 step. An optional critical shear stress for deposition (τ_d ; Pa; Krone, 1962; Whitehouse et al., 2000; Spearman and Manning,
213 2008; Mehta, 2014) has been implemented for cohesive sediment. Deposition in our model is zero when the bottom stress τ_b
214 (Pa) is greater than τ_d . When τ_b is less than τ_d , deposition increases linearly as τ_b decreases toward zero, behavior we call
215 linear depositional flux (Whitehouse et al., 2000; see Supplement). A simpler alternative is to assume a full settling flux
216 when $\tau_b < \tau_d$, which we call constant depositional flux, and which we have implemented as an option. According to
217 Whitehouse et al. (2000), τ_d is typically about half the magnitude of the critical shear stress for erosion τ_c , but is unrelated to
218 that value. Mehta (2014, Equation 9.83) suggested a relationship between τ_d for larger particles, using τ_d values for the
219 smallest particles in suspension and the ratio of diameters raised to an exponent that depends on sediment properties (see
220 Supplement), citing Letter (2009) and Letter and Mehta (2011). The effect of a critical shear stress for deposition is to keep
221 sediment in suspension in the bottom layer. This results in more material transported as suspended sediment and, for flocs,
222 allows aggregation and disaggregation processes to continue.

223 2.2.2. Fluxes out of the bed – Resuspension

224 Resuspension is modelled as an erosional mass flux $E_{s,i}$ from the top (active) bed layer to the bottom-most water column cell
225 (Ariathurai and Arulanandan, 1978; Warner et al., 2008) where

$$226 \quad E_{s,i} = E_{0,i} (1 - \phi) \frac{\tau_{sf} - \tau_{ce,i}}{\tau_{ce,i}}, \quad \text{when } \tau_{sf} > \tau_{ce,i} \quad (3)$$

227 where E_0 is a bed erodibility constant ($\text{kgm}^{-2} \text{s}^{-1}$), ϕ is porosity of the top bed layer, τ_{sf} is the skin-friction component of the
228 bottom shear stress (Pa), τ_{ce} is the effective critical shear stress (Pa), and i is an index for each sediment class. The total mass
229 eroded over a time step is limited by amount of that sediment class in the top layer of the bed. The skin-friction component
230 of the bottom shear stress is calculated using a wave-current bottom boundary layer model (Warner, 2008). The effective
231 critical shear stress for non-cohesive sediment depends on grain characteristics, but τ_{ce} for cohesive beds is a bulk property
232 of the bed, as discussed below in Section 2.5. The effective critical shear stress for mixed beds (i.e., non-cohesive grains in a
233 cohesive matrix) varies, as described below in Section 2.6.

234 2.4 Stratigraphy

235 Stratigraphy serves two functions in the model as conditions change and sediment is added or removed from the bed: (1) to
236 represent the mixture of sediment available at the sediment-water interface for use in bedload transport, sediment
237 resuspension, and roughness calculations; and (2) to record the depositional history of sediment. Bookkeeping methods for
238 tracking and recording stratigraphy must conserve sediment mass and must accurately record and preserve age, porosity, and
239 other bulk properties that apply to each layer. Ideally, a layer could be produced for each time step in which deposition
240 occurs, and a layer could be removed when cumulative erosion exceeds layer thickness. In practice, the design of many
241 models is subject to computational constraints that limit resolution to a finite and relatively small number of layers. In
242 ROMS, this number is declared at the beginning of the model run and cannot change. Thus, when deposition requires a new
243 layer, or when erosion removes a layer, other layers must be split or merged so that the total number of layers remains
244 unchanged. Where and when this is done determines the fidelity and utility of the modeled stratigraphic record. Some
245 models have used a constant layer thickness (Harris and Wiberg, 2001); others (for example, ECOMSED) define layers as
246 isochrons deposited within a fixed time interval (HydroQual, Inc., 2004). Our approach is most similar to that described by
247 Le Hir et al. (2011) in that we allow mixing of deposited material into the top layer, and require a minimum thickness of
248 newly formed layers, merging the bottom layers when a new layer is formed. Likewise, the bottom layer is split when
249 erosion or thickening of the active layer, discussed below, reduces the number of layers. The sequence of layer calculations
250 is described in detail in the Supplement.

251 A key component of the bed model is the active layer (Hirano, 1971), which is the thin (usually mm-scale), top-most layer of
 252 the seabed that participates in exchanges of sediment with the overlying water. During each model time step, deposition and
 253 erosion may contribute or remove mass from the active layer. Any stratigraphy in the active layer is lost by instantaneous
 254 mixing (Merkel and Klopmann, 2012), but this is consistent with the original concept of Hirano (1971) and the need to
 255 represent the spatially averaged surface sediment properties in a grid cell that represents a heterogeneous seabed. The
 256 thickness of the active layer in ROMS scales with excess shear stress (Harris and Wiberg, 1997; Warner et al., 2008) and is
 257 at least a few median grain diameters thick (Harris and Wiberg, 1997; see Supplement).

258 **2.5 Bulk Critical Shear Stress for Erosion for Cohesive Sediment**

259 An important difference between cohesive and non-cohesive sediment behavior is that the erodibility of cohesive sediment is
 260 treated primarily as a bulk property of the bed, whereas the erodibility of non-cohesive sediment is treated as the property of
 261 individual sediment classes. The erodibility of cohesive sediment often decreases with depth in the bed, resulting in depth-
 262 limited erosion (Type 1 behavior according to Sanford and Maa, 2001). When the cohesive bed module is used, the
 263 erodibility of cohesive beds depends on the bulk critical shear stress for erosion τ_{cb} (Pa), which is a property of the bed
 264 layer, not individual sediment classes, and generally increases with depth in the bed. It also changes with time through
 265 swelling and consolidation and, in the uppermost layer, is affected by erosion and deposition. The cohesive bed model tracks
 266 these changes by updating profiles of τ_{cb} at each grid point during each baroclinic timestep.

267 There is no generally accepted physically based model for determining τ_{cb} from bed properties such as particle size,
 268 mineralogy, and porosity. We adopted Sanford's (2008) heuristic approach based on the concept that the bulk critical shear
 269 stress profile tends toward an equilibrium profile that depends on depth in the seabed (Figure 1) and must be determined a
 270 priori. Erosion-chamber measurements (Sanford, 2008; Rinehimer et al., 2008; Dickhudt et al., 2009; Dickhudt et al., 2011;
 271 Butman et al., 2014) have been used to define equilibrium bulk critical shear stress profiles $\tau_{cb,eq}$ in terms of an exponential
 272 profile defined by a slope and offset.

$$273 \quad \tau_{cb,eq} = a \exp\left[\left(\ln(z_\rho) - offset\right) / slope\right] \quad (4)$$

274 where z_ρ (kg/m²) is mass depth, the cumulative dry mass of sediment overlying a given depth in the bed. In Equation 3, *offset*
 275 and *slope* have units of ln(kg/m²), and $a = 1 \text{ Pa kg}^{-1} \text{ m}^2$ is a dummy coefficient that produces the correct units of critical shear
 276 stress. The mass depth at the bottom of each model layer k is calculated as

$$277 \quad z_\rho(k) = \sum_k \sum_i f_{i,k} \rho_i \Delta z_k \quad (5)$$

278 where the summations are computed over the k bed layers and i sediment classes, f_i (dimensionless) is the fractional amount
 279 of sediment class i , ρ_i (kg/m³) is particle density in class i , and Δz_k (m) is the thickness of layer k . Equation 3 can be written
 280 in terms of the power-law fits to erosion-chamber measurements presented by Dickhudt (2008) and Rinehimer et al. (2008;
 281 see Supplement). The instantaneous bulk critical shear stress profile is nudged over time scale T_c or T_s (s) toward the
 282 equilibrium profile to represent the effects of consolidation or swelling following perturbations caused by erosion or
 283 deposition. T_c is the time scale for consolidation and is applied when the instantaneous profile is more erodible than the
 284 equilibrium value, while T_s is the time scale for swelling and is applied when the instantaneous profile is less erodible than
 285 the equilibrium value. The consolidation time scale is usually chosen to be much shorter than the one associated with
 286 swelling (Sanford, 2008). New sediment deposited to the surface layer is assigned a bulk critical shear stress that may either
 287 be (1) held constant at a low value (Rinehimer et al. 2008), or (2) set at the instantaneous bed shear stress of the flow.

288 **2.6 Mixed Sediment**

289 Mixed-sediment processes occur when both cohesive and non-cohesive sediment are present, and are typically sensitive to
 290 the proportion of mud. Beds with very low mud content (<3%; Mitchener and Torfs, 1996) behave as non-cohesive
 291 sediment: erodibility is determined by particle critical shear stress, which is an intrinsic characteristic of each particle class.
 292 Non-cohesive beds may be winnowed and armored by selective erosion of the finer fraction. In contrast, beds with more than
 293 3% to 15-30% (Mitchener and Torfs, 1996; Panagiotopoulos et al., 1997, van Ledden et al., 2004; Jacobs et al, 2011) mud
 294 content behave according to bulk properties that, in reality, depend on porosity, mineralogy, organic content, age, burial
 295 depth, etc., but that, in the model, are characterized by the bulk critical shear stress for erosion. Our approach to resuspension
 296 of mixed sediment is similar to that suggested by Le Hir et al. (2011) and Mengual et al. (2017). Mixed beds in the model
 297 have low to moderate mud content (3% to 30%, subject to user specification) and their critical shear stress in the model is a
 298 weighted combination of cohesive and non-cohesive values determined by the cohesive-behavior parameter P_c , which ranges
 299 from 0 (non-cohesive) to 1 (cohesive; see Supplement). Where $P_c = 0$, there is no cohesive behavior, and the particle shear
 300 stress τ_c for each sediment class is the effective critical shear stress τ_{ce} for that class. Where $P_c = 1$, the cohesive sediment
 301 algorithm is used, and the effective critical shear stress for each class is the greater of τ_c and the bulk critical shear stress
 302 τ_{cb} . Between those limits, the effective critical shear stress for each sediment class is

$$303 \quad \tau_{ce} = \max \left[P_c \tau_{cb} + (1 - P_c) \tau_c, \quad \tau_c \right] \quad (6)$$

304 This approach allows fine material (e.g., clay) to be easily resuspended when P_c is low and only a small fraction of mud is
 305 present in an otherwise sandy bed, and it limits the flux to the amount available in the active mixed layer. It also allows non-
 306 cohesive silt or fine sand embedded in an otherwise muddy bed to be resuspended during bulk erosion events when P_c is

307 high, and it provides a simple and smooth transition between these behaviors. The thickness of the active mixed layer is
 308 calculated as the thicker of the cohesive and non-cohesive estimates. Figure 2 illustrates mixed-bed behavior as the mud (in
 309 this case, clay-sized) fraction f_c increases for a constant bottom stress of 0.12 Pa. At low f_c , P_c is zero (Figure 2a), and clay
 310 and silt are easily eroded (high relative flux rates out of the bed; Figure 2c) because the particle critical shear stress for non-
 311 cohesive behavior of these fine particles is low (Figure 2b). The relative flux rates in Figure 2b are normalized by the
 312 fractional amount of each class and the erosion-rate coefficient; the actual erosional fluxes for clay content would be low at
 313 $P_c = 0$ because of the low clay content in the bed. As f_c increases and the bed becomes more cohesive, relative erosion flux
 314 rates decline. When f_c exceeds a critical value (0.2 in the example shown in Figure 2), the bed is completely cohesive and
 315 erosion fluxes are determined by bulk critical shear stress for erosion of cohesive sediment τ_{cb} .

316 Non-cohesive sediment classes are subject to bedload transport when the bottom stress exceeds both the bulk critical shear
 317 stress of the top (active) layer and the particle critical shear stress for that class. In these cases, the transport-rate equations
 318 still calculate bedload transport based on excess shear stress associated with the non-cohesive particle critical shear stress, as
 319 described in Warner et al (2008). Cohesive classes are not subject to bedload transport; if the bulk critical shear stress of the
 320 bed is exceeded, we assume they will go directly into suspension.

321 **2.7 Bed Mixing**

322 Mixing of bed properties in sediment can be caused by benthic fauna (ingestion, defecation, or motion such as burrowing) or
 323 circulation of porewater, and tends to smooth gradients in stratigraphy and move material vertically in sediment. The model
 324 (e.g., Boudreau, 1997) assumes that mixing is a one-dimensional vertical diffusive process and neglects non-local and lateral
 325 mixing processes:

$$326 \quad \frac{\partial C_v}{\partial t} = \frac{\partial}{\partial z} \left(D_b \frac{\partial C_v}{\partial z} \right) \quad (7)$$

327 where C_v is the volume concentration of a conservative property (e.g., fractional concentration of sediment classes or
 328 porosity), D_b is a (bio)diffusion coefficient (m^2/s) that may vary with depth in the bed (see below), and z (m) is depth in the
 329 bed (zero at the sediment-water interface, positive downward). We have discretized Equation (7) using the varying bed
 330 thicknesses and solve it at each baroclinic time step using an implicit method that is stable and accurate (See Supplement).

331 Biodiffusivity is generally expected to decrease with depth in the sediment (Swift et al., 1994; 1996), but is often assumed to
 332 be uniform near the sediment-water interface. The typical depth of uniform mixing, based on worldwide estimates using
 333 radionuclide profiles from cores, is 9.8 ± 4.5 cm (Boudreau, 1994). Rates of biodiffusion estimated from profiles of excess

334 ^{234}Th on a muddy mid-shelf deposit off Palos Verdes (California, USA) varied from $\sim 2 \text{ cm}^2/\text{yr}$ to $\sim 80 \text{ cm}^2/\text{yr}$ (Wheatcroft
335 and Martin, 1996; Sherwood et al., 2002) and values from the literature range from $0.01 - 100 \text{ cm}^2/\text{yr}$ (Boudreau, 1997;
336 Lecroart et al., 2010). The depth-dependent biodiffusion rate profile in the model must be specified for each horizontal grid
337 cell using a generalized shape described in the Supplement.

338 Representation of seabed properties, i.e. the stratigraphy, has been modified slightly from the framework presented in
339 Warner et al. (2008). The revised bed model gives the user latitude to control the resolution of the bed model through the
340 choice of new layer thickness and the number of bed layers, and avoids the mixing described by Merkel and Klopmann
341 (2012). The bookkeeping for bed layers is detailed in the Supplement. The main differences from previous versions of the
342 model (Warner et al., 2008) are the treatments of the second layer (immediately below the active layer) and the bottom layer.
343 During deposition, the new algorithm prevents the second layer from becoming thicker than a user-specified value, which
344 results in thinner layers that can record changes in sediment composition inherited from the active layer as materials settle.
345 During erosion, the new algorithm splits off only a small portion of the bottom layer to create a new layer. This limits the
346 influence of the initial stratigraphy specified for the bottom layer and confines blurring of the stratigraphic record to the
347 bottommost layers. Our tests indicate the new approach provides a more informative record of stratigraphic changes.
348 Moriarty et al. (2017) used a similar approach to bed stratigraphy to preserve spatial gradients in sediment biogeochemistry.

349 **3 Demonstration Cases**

350 The following cases demonstrate the cohesive-sediment processes included in ROMS, explore model sensitivity to
351 parameters, and provide candidates for inter-model comparisons.

352 **3.1 Floc Model**

353 Tests using a quasi one-dimensional vertical implementation of ROMS were conducted to verify that the floc model was
354 implemented correctly and to gain some insight into model behavior under typical coastal conditions.

355 **3.1.1 Comparison with laboratory experiments**

356 Verney et al. (2011) compared results from FLOCMOD with a laboratory experiment of tidal-cycle variation in shear rate G .
357 We performed the same simulations in ROMS by initializing with the same floc model parameters. The model was run with
358 15 cohesive classes (instead of the 100 classes in the reference FLOCMOD experiment). Settling velocities were set to zero,
359 and the turbulent shear parameter $G(t)$ was specified, ranging from $G=0 \text{ s}^{-1}$ at slack tide to $G=12 \text{ s}^{-1}$ at peak flow. Periodic
360 lateral boundary conditions were used, effectively creating a zero-dimensional simulation where the only active process was

361 flocculation response to the changing turbulent shear. The class sizes were log-spaced between 4 and 1500 μm with flocculation densities
 362 derived from Equation 1 using $n_f = 1.9$. The suspended-sediment concentration was constant at 0.093 kg/m^3 , and it was
 363 initially all in the 120- μm class. Our results (Figure 3a) matched the cycles of flocculation diameter variation caused by aggregation
 364 (low G) and breakup (high G) shown in Figure 7 of Verney et al. (2011), with a 24- μm root-mean square (rms) difference
 365 from observations in mass-weighted mean diameter. As in the Verney et al. (2011) simulation, our model did not reproduce
 366 the dip in mean grain diameter at ~ 400 min, which may have been caused by settling of the larger flocs in the laboratory
 367 experiment.

368 We also compared our ROMS FLOCMOD implementation with laboratory experiments of the growth and breakup of flocs
 369 performed by Keyvani and Strom (2014) who used a constant sediment concentration of 0.05 kg/m^3 and applied cycles of
 370 $G=15 \text{ s}^{-1}$ that caused flocculation growth followed by long periods (15 h) of very strong turbulent shear rates ($G=400 \text{ s}^{-1}$) that caused
 371 disaggregation. We simulated the first cycle of flocculation formation using the size classes, fractal dimension, and concentrations
 372 provided by Keyvani and Strom (2014), but varying the aggregation parameter α and the breakup parameter β that determine
 373 the final equilibrium diameter. Our model results with $\alpha=0.1$ and $\beta=0.0135$ (Figure 3b) reproduced the observations with
 374 higher skill than the simple model used in their study. The same final diameter was obtained with $\alpha=0.45$ and $\beta=0.06$, but the
 375 equilibrium was attained more quickly than observed.

376 These comparisons with laboratory results indicated that our implementation of FLOCMOD in ROMS was correct and
 377 demonstrated that the model has useful skill in representing flocculation dynamics.

378 **3.1.2. Comparison to equilibrium flocculation size**

379 Simulations were conducted to further evaluate the ROMS implementation of FLOCMOD by comparing modeled
 380 equilibrium flocculation sizes to equilibrium flocculation sizes predicted by Winterwerp (2006). He argued that, in steady conditions,
 381 equilibrium flocculation sizes are determined by the fractal dimension n_f , ratio of aggregation rates and breakup rates, concentration
 382 C (kg/m^3), and turbulence shear rate G (s^{-1}). The equilibrium median flocculation size D_{50} (m) is given by

$$383 \quad D_{50} = D_p + \frac{k_A}{k_B} \frac{C}{\sqrt{G}} \quad (8)$$

384 where k_A and k_B are aggregation and breakup coefficients, respectively (Winterwerp, 1998). The units of k_A and k_B depend on
 385 fractal dimensions, but the ratio has units of $\text{m}^4\text{kg}^{-1}\text{s}^{-1/2}$. We compared our FLOCMOD results with this theoretical
 386 relationship by running cases with steady conditions, $n_f = 2$, for a range of concentrations ($C = 0.1$ to 10 kg/m^3), a range of
 387 shear rates ($G = 0.025$ to 100 s^{-1}), and several combinations of aggregation and breakup parameters α and β . The results show

388 that equilibrium floc size increases with concentration and decreases with turbulence shear rate, as expected (Figure 3c).
389 Equilibrium diameter is strongly controlled by concentration, and turbulence is more effective at reducing average diameter
390 at lower concentrations. The slope of the relationship between the equilibrium diameter and C / \sqrt{G} varies with the ratio of
391 aggregation to breakup. Winterwerp (1998) suggested a slope of about $4 \times 10^3 \text{ m}^4 \text{ kg}^{-1} \text{ s}^{-1/2}$. Figure 3c demonstrates that a range
392 of slopes can be obtained by varying the ratio α/β . The model reproduced the linear response predicted by Winterwerp
393 (1998) except near the largest sizes, where our upper limit in floc class size (5000 μm) distorted the statistics. Although not
394 shown in Figure 3c, the floc populations evolved at different rates, depending on α and β , as indicated in Figure 3b.

395

396 3.1.3. Evolution to steady state

397 Steady, uniform flow is a conceptually simple model test that demonstrates the hydrodynamics linking vertical profiles of
398 flow, evolution of the turbulent boundary layer, and bottom drag. The addition of floc dynamics creates a complicated and
399 instructive test case. The model set-up was a fully three-dimensional implementation with advection, diffusion, and settling
400 of the dynamically changing floc population. The vertical grid included 40 cells, but the horizontal aspect of the grid was
401 small (5 cells...just enough to accommodate the templates of the finite-difference formulations) and included lateral periodic
402 boundary conditions, so that anything advected out of the domain re-entered on the upstream side. This simulation, forced by
403 a constant sea-surface slope, is similar to the steady flow test examined by Winterwerp (2002, section 4.8.1), and produces a
404 linear Reynolds-stress profile increasing from zero at the surface to $\tau_b = -\rho_w g h ds/dx$ at the seabed, where τ_b (Pa) is
405 bottom shear stress, g (m/s^2) is gravitational acceleration, h (m) is water depth, and ds/dx (m/m) is sea-surface slope. The
406 flow develops a logarithmic velocity profile $u = (u_* / \kappa) \ln(z / z_0)$, where u (m/s) is velocity in the x direction,
407 $u_* = \sqrt{\tau_b / \rho_w}$ is shear velocity (m/s), $\kappa = 0.41$ (dimensionless) is von Kármán's constant, z (m) is elevation above the bed,
408 and z_0 (m) is the bottom roughness length. The final flow velocity near the surface is about 0.6 m/s. When non-cohesive
409 sediment is added (and erosion and deposition are set to zero), the suspended sediment concentrations for each size class
410 evolve into Rouse-like profiles where, at each elevation, downward settling is balanced by upward diffusion. The addition of
411 floc dynamics complicates the situation, because aggregation creates larger flocs with higher settling velocities. The larger
412 flocs tend to settle into regions of higher shear and higher concentration, where the higher shear tends to break them into
413 smaller flocs but the higher concentrations enhance aggregation. The size distribution, settling velocity, concentration, shear,
414 and turbulent diffusion evolve to a steady state under a dynamic balance. The resulting profiles of concentration and mass-
415 weighted average size and settling velocity are sensitive to both floc model parameters and modeled physical conditions
416 (water depth, bottom stress, turbulence model, total sediment in suspension).

417 We demonstrate this process using 22 floc classes with logarithmically spaced diameters ranging from 4 to 5000 μm (Figure
418 4). The initial vertical concentration profile was uniform at 0.2 kg/m^3 , all in the $8\text{-}\mu\text{m}$ class. The model started from rest, and
419 the initial response was slow particle settling in the nearly inviscid flow: concentrations, floc sizes, and settling velocities all
420 decreased near the surface (Figures 4a, b, and c). As the flow accelerated in the first two hours, turbulence generated by
421 shear at the bottom began to mix upward in the water column, diffusing settled material higher and facilitating collisions and
422 aggregation among flocs. Between hours 3 and 4, settling was enhanced by these newly formed larger flocs, as is apparent in
423 increases in average diameter and settling velocities, and reduced concentrations near the surface. Equilibrium was nearly
424 established by about hour 5. At the end of the model run, the total concentration profile decreased exponentially with
425 elevation (Figure 4d and 4g), but average size and settling velocities both decreased markedly in the bottom meter (Figures
426 4e and 4f), reflecting shear disaggregation that lead to increases in smaller flocs near the bottom (Figure 4g).

427 The time scales to achieve equilibrium in this simulation are comparable to tidal time scales, suggesting equilibrium is
428 unlikely in the real world, where forcing is time dependent and bottom conditions are spatially variable. The final condition
429 is sensitive to flow forcing, initial concentrations, and floc parameters. For example, when concentrations are higher, or
430 when the disaggregation parameter is increased (making the flocs more fragile), bottom-generated shear causes
431 disaggregation higher into the water column, and mid-depth maxima in diameter and settling velocity evolve. This steady
432 flow simulation is useful as both a standard test case and a reminder of the complexity of floc processes, even when the
433 hydrodynamics are relatively simple.

434 **3.1.4. Settling fluxes**

435 Interaction with the bed influences the evolution of the floc population in the water column by providing sources or sinks in
436 various size classes. We have experimented with several sediment-flux conditions from the water column to the seabed,
437 including settling fluxes, zero fluxes, and fluxes modulated by threshold stresses for deposition. Settling fluxes calculated as
438 $w_k \rho_k C_k \Delta t$ summed over each class k , is the default method used for non-cohesive sediment. Zero-flux boundary conditions
439 essentially treat the bottom water-column cell as a fluff layer, allowing flocs to accumulate by settling or mix out by
440 diffusion. Floc dynamics continue to operate in this layer, so the size distributions change with concentration and stress.
441 Settling fluxes modulated by stress thresholds for deposition allow flocs to deposit only under relatively quiescent
442 conditions. The model framework provides a variety of choices described in the Supplement, each with implications that
443 must be assessed in the context of the problem at hand. As expected, the conditions that reduced settling into the bed resulted
444 in higher sediment concentrations in the bottommost water-column layer and allowed for floc breakup by the enhanced near-
445 bottom turbulence.

446 **3.1.5. Model sensitivity**

447 A wide range of model runs (not presented here) have provided us with a qualitative sense of model performance. Model
448 results respond as expected to physical parameters, such as mean concentration and shear rate (discussed above), as well as
449 primary particle size and fractal dimension. Model results are also sensitive to model configuration, including the number of
450 size classes, the size of vertical grid spacing, and the time step used. Our experience so far confirms that of Verney et al.
451 (2011): a truncated distribution of about seven size classes provides qualitatively useful results, but the choice of size range
452 and size distribution may change the results. The sensitivity to vertical grid resolution is particularly important in the
453 bottommost layer, which has the highest concentrations and highest shear rates. Finer grid spacing near the bottom results in
454 layers with higher shear and higher sediment concentrations, which cause local changes in the equilibrium floc sizes. Model
455 time steps in our floc model tests are short, ranging from 10 to (more typically) 1 s. The adaptive sub-steps for aggregation
456 and disaggregation were limited to a minimum of 0.5 s. At high concentrations ($> 0.2 \text{ kg/m}^3$) and high shear rates, the results
457 sometimes showed numerical instability, probably related to the explicit solution of Equations 2. Replacement of the solver
458 for these equations with a faster and more robust method in the future should improve model stability.

459 **3.2 Resuspension**

460 Three cases are presented here to demonstrate the evolution of stratigraphy caused by resuspension and subsequent settling
461 of sediment during time-dependent bottom shear stress events. They contrast model calculations using the non-cohesive and
462 mixed-bed routines, and highlight the role of biodiffusion. These were one-dimensional (vertical) cases represented with
463 small ($\sim 5 \times 6$ horizontal $\times 20$ vertical cells), three-dimensional domains with flat bottoms and periodic lateral boundary
464 conditions on all sides. They were forced with time-varying surface wind stress that generated time-dependent horizontal
465 velocities and bottom stress, initialized with zero velocity and zero suspended-sediment concentration, and did not include
466 floc dynamics in the water column.

467 **3.2.1 Non-cohesive bed simulation**

468 A non-cohesive bed simulation with a water depth of 20 m and periodic boundary conditions was used to demonstrate the
469 generation and preservation of sand and silt stratigraphy during a resuspension and settling event (Figure 5). The model was
470 forced with two stress events ~ 1.5 d apart and lasting 1.5 d and 1 d respectively. Four sediment classes, representing
471 particles with nominal diameters of 4, 30, 62.5, and 140 μm , particle critical shear stresses of 0.05, 0.05, 0.1, and 0.1 Pa, and
472 settling velocities of 0.1, 0.6, 2, and 8 mm s^{-1} were used. Although the diameters of the first two sediment classes
473 corresponded to mud, all sediment classes in this experiment were treated as non-cohesive material. The initial sediment bed

474 contained 41 layers, each 1 mm thick, and each holding equal fractions (25%) of the four sediment classes. New sediment
475 layers were constrained to be no more than 1 mm thick.

476 The first, larger stress event (maximum $\tau = 1$ Pa; Figure 5b), eroded 1.2 cm of bed, and expanded the active layer to a
477 thickness of 0.8 cm, so the bed was disturbed to a depth of 2 cm. Expansion of the active layer homogenized enough layers
478 to provide 0.8 cm of sediment, making more fine sediment available for resuspension. The finer fractions dominated the
479 suspended sediment in the water column, which contained only a small fraction of the coarsest sand (Figure 5a). When the
480 stress subsided, coarser sediment deposited first, while finer material remained suspended, producing thin layers of graded
481 bedding above the 2-cm limit of initial disturbance (Figure 5d).

482 The second stress pulse eroded the bed down to 1 cm but only resuspended minimal amounts of the 140- μm sand.
483 Deposition resumed after the second pulse subsided and, at the end of the simulation, some mud remained in the water
484 column (Figure 5a), leaving the bed with net erosion of 5 mm (Figure 5d). The finest material (4 μm) remained mostly in
485 suspension after five days. The final thickness of the bottom five layers was smaller than their initial value (1 mm), because,
486 to maintain a constant number of bed layers, the deepest layer was split each time a surface layer was formed during
487 deposition. The two stress pulses affected sediment texture down to 2 cm. Above this level, almost all of the finest class was
488 winnowed, and remained mostly in suspension while the other classes settled to the bed, so that the upper bed layers
489 developed a fining-upward storm layer. The bottom portion of the storm layer (1 – 2 cm depth) was a lag layer comprised of
490 the two coarsest classes, both because these resisted erosion and because the sand that did erode settled to the bed quickly
491 when shear stress decreased.

492 **3.2.2 Mixed bed simulation**

493 This case examined the stratigraphic consequences of cohesive behavior resulting from a single bottom-stress event (Figure
494 6). The model configuration was similar to the previous example. The same sediment classes were used, but the two finest (4
495 and 30 μm) were treated as cohesive mud, while the other two remained non-cohesive (sand). The fraction of cohesive
496 sediment ($f_c = 0.5$) exceeded the chosen non-cohesive threshold (f_{nc} threshold = 0.2), so the bed behaved as if it were
497 completely cohesive. The cohesive formulation required the initialization of an equilibrium bulk critical stress profile for
498 erosion. We chose parameters within the range of sensitivities studied by Rinehimer et al. (2008) and specified an
499 equilibrium profile with a slope = 2 $\ln(\text{kg}/\text{m}^2)$ and an offset of 3.4 $\ln(\text{kg}/\text{m}^2)$, with a minimum value of 0.03 Pa and a
500 maximum of 1.5 Pa (dashed magenta line in Figure 6b) and initialized the model with this profile (solid purple line in Figure
501 6b). The time scale for consolidation was set to $T_c = 8$ hours. The swelling time scale was chosen to be 100 times longer than
502 consolidation ($T_s = 33$ days). A time series of bed stress was imposed (Figure 6a), and the bed responded initially by

503 eroding. As the imposed stress waned starting at day 37, sediment settled to the bed causing deposition. The initial rapid
504 increase in bottom stress during the first 0.7 days (Figure 6a) exceeded the critical stress of the bed to a depth of 2.4 cm (red
505 line in Figure 6c), causing resuspension and erosion of the top 5 mm of the bed. In this case, the amount of material eroded
506 was limited by the erosion rate coefficient. The equilibrium critical stress profile, which has a static shape, shifted down with
507 the sediment-water interface (compare dashed magenta line in Figures 6b, c). After the initial erosion, the instantaneous
508 critical stress profile tended toward the equilibrium critical stress profile over the slow swelling time scale of 33 days,
509 rendering the bed progressively more erodible (compare Figures 6c, d). The process of swelling, while slow, rendered the
510 bed more erodible, and an additional 2-3 mm of sediment was removed by day 32. By day 38, the stress had waned and 4
511 mm of sediment had redeposited (Figure 6d). The equilibrium critical stress profile had shifted upward with the bed surface,
512 causing the instantaneous critical stress to increase over the short compaction time scale. The final instantaneous critical
513 shear stress profile (Figure 6e) had almost reached the long-term equilibrium everywhere except in the most recent deposits.
514 This case exemplifies the sequence of depth-limited erosion, deposition, and compaction that characterizes the response of
515 mixed and cohesive sediment in the model.

516 **3.2.3 Biodiffusion simulations**

517 We validated the numerical performance of the biodiffusion algorithms using two analytical test cases with a realistic range
518 of parameters. The implicit numerical solution is unconditionally stable and conserves mass to within 10^{-8} %, but the
519 accuracy depends on time step, gradients in biodiffusivity, and bed thickness. Typical RMS differences in the fractional
520 amount of sediment in a particular class between the numerical solutions and the analytical solutions ranged from 10^{-2} to 10^{-6} .
521 We found that, for modeled beds 5 m thick, solutions improved as layer thickness decreased from 50 to 5 cm, but beyond
522 that, higher resolution did not substantially improve the solution. Even in the worst case, where the numerical solution was
523 off by 1%, it was much more precise than our estimates of biodiffusivity coefficients.

524 Four cases are presented to demonstrate bed mixing (Figure 7). The first two used the same configuration as in the non-
525 cohesive (Figures 5, 7a) and mixed-bed simulations (Figures 6d, 7b). The second two were identical to the mixed-bed case
526 except that biodiffusive mixing was enabled. The biodiffusivity profile used was similar to that proposed for the mid-shelf
527 deposit offshore of Palos Verdes, CA (Sherwood et al., 2002) that had a constant diffusivity D_{bs} from the sediment-water
528 interface down to 2 mm, an exponential decrease between 2 mm and 8 mm, and a linear decrease to zero at 1 cm depth.
529 These two cases differed in their biodiffusion coefficients: a) the first used relatively large biodiffusion coefficients ($D_{bs} =$
530 $10^{-5} \text{ m}^2\text{s}^{-1}$); b) the second used smaller values ($D_{bs} = 10^{-10} \text{ m}^2\text{s}^{-1}$).

531 The resulting stratigraphy after the five-day simulation (Figure 7) indicates that mixing in the case with large biodiffusivity
532 (Figure 7c) tended to smooth all gradients rapidly and only during depositional conditions was the vertical structure of grain
533 size fractions preserved. Some sediment remained in suspension in all four cases, which was reflected in the final bed
534 elevation. The resulting top 1 cm of the bed was always well mixed and the depth of the disturbed sediment at the end of the
535 simulation was deeper (2.5 cm) in this case than in the other simulations. Sediment deeper than 2.5 cm below the surface was
536 undisturbed: it was beyond the reach of erosion, active-layer formation, and biodiffusion. The biodiffusive mixing increased
537 recruitment of fine sediment into the surface active layer during erosion, resulting in increased concentrations in the water
538 column (not shown) compared to the mixed bed case without biodiffusion.

539 The case with a smaller biodiffusion coefficient (Figure 7d) developed stratigraphy intermediate to those cases with large
540 and zero biodiffusion. The depth of disturbed sediment was 2.3 cm and the transition between redeposited sand and mud was
541 smooth with coarse sand being present at the surface of the bed. This gradual size gradation was intermediate to the sharp
542 jump in the fractional distribution between mostly sandy layers and predominantly muddy layers produced in cases that
543 neglected mixing (Figure 7a,b) and the smooth gradient produced by the strong mixing case (Figure 7c).

544 **3.3 Estuarine Turbidity Maxima**

545 High concentrations of suspended sediment often occur near the salt front in estuaries, forming estuary turbidity maxima
546 (ETM). We present ETM test cases that simulated sediment transport in a two-dimensional (longitudinal and vertical) salt-
547 wedge estuary with tidal and riverine forcing. The cases investigated the formation of cohesive deposits beneath the ETM
548 with and without floc dynamics. The first case, without floc dynamics but with a mixed bed, is presented here. The second
549 case, presented below, adds floc dynamics. The model was forced with a 12-hour tidal oscillation modulated with a 14-day
550 spring-neap cycle. The idealized estuary was 100-km long with a sloping bottom 4 m deep at the head of the estuary and 10
551 m deep at the mouth (Figure 8a). In all cases, the simulations were run for twenty tidal cycles. Two non-cohesive sediment
552 classes (180- and 250- μm diameter) were represented with equal initial bed fractions (50% of each). One cohesive fraction
553 (37 μm , $\rho_f = 1200 \text{ kg/m}^3$, $w_s = 0.13 \text{ mm/s}$) was included, with an initial uniform suspended-sediment concentration of 1
554 kg/m^3 . The bed was initialized without any cohesive sediment, so it initially behaved non-cohesively. Later in the simulation,
555 bed behavior became mixed as suspended mud settled and was incorporated into the initially sandy bed. The chosen
556 equilibrium bulk critical shear stress profile (Equation 3) had *slope* = 5 $\ln(\text{kg/m}^2)$ and *offset* = 2 $\ln(\text{kg/m}^2)$, with a minimum
557 value of 0.05 Pa and a maximum of 2.2 Pa. The time scale for consolidation was set to $T_c=8$ hours (Sanford, 2008;
558 Rinehimer, 2008), and the swelling time scale was set to $T_s=33$ days.

559 During the simulations, salinity and suspended-sediment field evolved into dynamic equilibria that were repeated over
560 consecutive tides. An estuarine turbidity maximum (ETM) developed between 10 km and 60 km from the mouth of the

561 estuary (Figure 8a) in the salt wedge generated by gravitational circulation and tidal straining (Burchard and Baumert, 1998;
562 MacCready and Geyer, 2001). Elevated suspended-sediment concentrations ranging from 0.7 to 2.05 kg/m³ occupied most of
563 the bottom layer and extended to mid-depth. No floc dynamics were included, so all of the suspended material depicted in
564 Figure 8a was in the 37- μ m class.

565 The second case was identical, except that it included floc dynamics. Fifteen cohesive (floc) classes and the two non-
566 cohesive (sand) classes were included. Floc-class diameters were logarithmically spaced, ranging from 20 to 1500 μ m, with
567 floc densities ranging from 1350 to 1029.3 kg/m³, and settling velocities ranging from 0.078 to 5.31 mm/s, commensurate
568 with Equation 1 with fractal dimension $n_f = 2$. The suspended-sediment concentration field was initialized with a uniform
569 concentration of 1 kg/m³, all in the 37- μ m class. The resulting ETM (Figure 8b) extended farther up-estuary and contained
570 much lower concentrations (0.1 to 0.5 kg/m³ in most of the salt wedge, with a thin layer of higher concentrations (2.1 kg/m³)
571 in the bottom layer (bottom 5% of the water column). The second layer (5 – 10% of the water column) had concentrations
572 about half of the bottom layer. The bed sediment response for the two cases also differed. In the no-floc case, the ETM
573 deposit was slightly thinner, located closer to the mouth, and varied less from slack to flood (Figure 8c). Floc dynamics
574 created large tidal variations in the size of bed material (Figure 8d), which ranged up to 600 μ m as flocs deposited during
575 slack, and decreased to 37 μ m as flocs were resuspended during flood. The behavior in the unflocculated case was less
576 intuitive. Over the course of the simulation, enough fine material accumulated beneath the ETM to cause the bed to behave
577 cohesively, but the top, active layer remained mostly non-cohesive. During flood tide, bottom stresses were sufficient to
578 resuspend the non-cohesive 70 μ m material, leaving the cohesive 37 μ m material on the bed. Thus, in both cases, the bed
579 became finer during period of higher stress, but for different reasons. The two cases highlight the model-dependent changes
580 in location (driven primarily by settling velocities) and size distributions (driven by floc dynamics) of the ETM.

581 We next expanded the numerical experiment, using six floc cases to elucidate the effects of floc dynamics in the idealized
582 estuary (Table 1). The two-dimensional model domain was the same as the ETM case described above. Three types of floc
583 behavior in the seabed were investigated: (1) no changes in size distribution occurred in the bed; (2) the floc evolution
584 process in the bed was invoked, which nudged all cohesive sediment into the 20- μ m class over a long time scale (50 hours);
585 and (3) the floc evolution process was invoked with a short time scale (5 hours). Additionally, three other combinations of
586 aggregation (α) and disaggregation (β) rates were used with the slow floc evolution in the bed rate to explore floc
587 processes in the water column (Table 1). The following six metrics were compared at the location of the maximum depth-
588 mean suspended-sediment concentration (SSC): depth-mean SSC; maximum SSC; median size (D_{50}); 12-h mean of the D_{50} ;
589 depth-mean settling velocity w_s ; and depth-mean w_s averaged over a 12-h tidal period (Table 1). The median size and mean

590 settling velocities were weighted by the mass in each class. Also listed in Table 1 are the locus of the maximum deposition,
591 the thickness at that location, and the median size of deposited material at that location.

592 Mean SSC in the ETM did not vary significantly among the floc cases, but the maximum SSC (located lower in the water
593 column) increased when the ratio of aggregation rate / disaggregation rate α / β was higher, which led to larger, faster-
594 settling flocs. Among the four cases (3 – 6) with slow floc evolution rates in the bed, settling velocities, maximum SSC, and
595 floc size covaried. The locus of maximum deposition of ETM material was insensitive to the algorithms for floc evolution in
596 the bed (cases 1 – 3), and most sensitive to the overall floc rates. The range of ETM locations is listed in Table 6 to highlight
597 the cases where ETM location varied. The case with lowest floc rates (case 5) produced the farthest upriver deposit, with the
598 most variation in the location of the maximum. The case with the highest settling velocities (case 6) produced deposits
599 closest to the estuary mouth. Overall, the simulated ETM was more sensitive to changes in floc parameters than to prescribed
600 behavior of the floc evolution in the seabed, and the greatest effect of varying floc dynamics was the vertical location of the
601 ETM, which was controlled by floc size and settling velocity.

602 **4 Realistic Application: York River Estuary**

603 This section demonstrates the cohesive sediment bed model in a realistic domain representing the York River, a sub estuary
604 of Chesapeake Bay (Figure 9). Recent modeling efforts have focused on this location as part of a program aimed at exploring
605 links between cohesive sediment behavior, benthic ecology, and light attenuation. As part of this program, colleagues have
606 obtained complementary field observations there, which have been especially focused on the two locations off Gloucester
607 Point and Clay Bank, VA (e.g. Dickhudt et al. 2009, 2011; Cartwright et al. 2013). The implementation presented here is
608 similar to the three-dimensional model developed by Fall et al. (2014) that accounted for circulation, sediment transport, and
609 a cohesive bed. While this model neglects flocculation, information obtained by field observations such as Cartwright et al.
610 (2013) have been consulted for guidance in setting settling velocities of the cohesive particles. The model is run assuming
611 muddy behavior of the bed, and neglecting mixed bed processes, because the majority of sediment transport within the York
612 River channels consists of fine-grained material. We found that it was important to modify the sediment bed layering
613 management scheme, as discussed in section 5 below, to resolve the high gradients in bed erodibility evident in the sediment
614 bed model (i.e. Fall et al 2014) and data (i.e. Dickhudt et al. 2009, 2011).

615 In this implementation, sediment deposited to the bed provided an easily erodible layer with an assumed low critical stress, τ_c
616 = 0.05 Pa. The modeled sediment bed erodibility and suspended-sediment concentrations both were found to be sensitive to
617 parameterization of the equilibrium critical stress profile, and to the consolidation and swelling timescales used (Fall et al.,

618 2014). Here we present a case similar to that shown by Fall et al. (2014), but that differs mainly in terms of the sediment bed
619 initialization. The equilibrium critical stress profile was chosen as $\tau_{cbeq} = z_p^{0.62}$ which was a power-law fit of erodibility
620 experiments performed by Dickhudt (2008) on field-collected cores in September 2007 (Rinehimer et al., 2008). Swelling
621 and consolidation timescales of 1 day and 50 days, respectively, were used. Both the porosity ($\phi = 0.9$) and the erosion rate
622 parameter $E_0 = 0.03 \text{ kg}/(\text{m}^2 \text{ s Pa})$ were held constant. A zero-gradient condition was applied for suspended-sediment
623 concentration at the open boundary where the York River meets Chesapeake Bay. Six sediment classes that had settling
624 velocities ranging from 0.032 to 10 mm/s were used. To initialize the seabed, they were distributed in equal fractions
625 throughout the model domain in a 20-layer sediment bed that had a total thickness of 1 m, with all but the bottom layer being
626 thin (0.1 mm). In this way, the model was initialized with a sediment bed that had high vertical resolution (0.1 mm) in the
627 upper ~2 cm, underlain by a thick layer (~1 m) sediment. This created high vertical resolution in the bulk critical shear stress
628 profile near the sediment – water interface, while still providing a fairly large pool of sediment so that erosional locations
629 retained some sediment in the seabed throughout the model run. Bed critical stress was initialized everywhere to be constant
630 (0.05 Pa) with depth, and quickly evolved to the equilibrium critical shear stress profile at the compaction time scale of a few
631 days. The model was run to represent two months using the sixty-year median freshwater flow of $67 \text{ m}^3/\text{s}$ and a spring-neap
632 tidal cycle with 0.2-m neap amplitude and 0.4-m spring amplitude.

633 The initially uniform bed evolved during the 60-day model run, developing areas of high sediment erodibility along the
634 shoals of the estuary and channel flanks (Figure 10a). In general, sediment was removed from the main channel, which
635 developed reduced erodibility (Figure 10a). At the Gloucester Point site, the initial bed evolved to become less erodible, with
636 a critical shear stress at the seabed that exceeded the equilibrium values specified for the model (Figure 10a). Conversely, at
637 the Clay Bank field site, conditions were variable in space. Sediment deposited on the shoal area, which evolved to enhanced
638 erodibility (Figure 10a). Within the channel, however, the equilibrium critical stress for erosion was often exceeded,
639 resulting in a strongly eroded sediment bed having larger values of critical shear at the sediment surface (Figure 10a).
640 Resuspension and transport also changed the spatial distribution of sediment classes, with the erosional areas retaining only
641 the coarser, faster-settling classes, while depositional areas retained finer-grained, slower-settling particles (Figure 10 b, c).
642 These patterns, with coarse lag layers and reduced erodibility in the channels relative to the shoals, are consistent with the
643 known grain size distributions and properties of the York River Estuary.

644 **5 Discussion**

645 The model algorithms presented here were motivated by the need to improve the representations of sediment dynamics in
646 numerical models of fine-grained and mixed-sediment environments. The improvements were implemented in the COAWST

647 version of ROMS, which provides a framework for realistic two-way nested models with forcing from meteorology (WRF;
648 Michalakes et al., 2001) and waves (either SWAN: Booij et al., 1999; or WaveWatch III; Tolman et al., 2014). Waves, in
649 particular, play an important role in cohesive sediment dynamics through wave-enhanced bottom shear stresses, wave-
650 induced near-bottom turbulence, and wave-induced nearshore circulation, but wave-induced fluid-mud layer processes are
651 not represented. ROMS includes options for several turbulence sub-models (e.g., $k - \varepsilon$, $k - \omega$, Mellor-Yamada) and wave-
652 current bottom-boundary layer sub-models that allow us to calculate fields of shear velocity G . Implementation of
653 FLOCMOD in this framework provides a platform for numerical experiments and real-world applications of a full-featured
654 floc model.

655 The primary role of the floc model is to simulate the dynamical response of particle settling velocities to spatial and temporal
656 variations in shear and suspended-sediment concentrations. This can also be achieved with simpler and computationally
657 more efficient parameterization in many applications. What are the advantages of the complex and much slower model
658 implemented here? There are several. The floc model provides fields of particles with dynamically varying density and
659 number of primary particles, which allow calculation of the acoustic and optical responses of the particle fields. In turn, this
660 allows direct comparison with field measurements of light attenuation, optical backscatterance, and acoustic backscatterance,
661 the de facto proxies for suspended-sediment concentration. This also allows calculation of derived properties in the water
662 column, including light penetration and diver visibility. Finally, the modeled particle properties can be used in geochemical
663 calculations that require estimates of particle radius, porosity, and reactive surface area. Depending on the application, this
664 additional information may justify the computational expense of the floc model.

665 The cohesive bed model provides a heuristic but demonstrably useful tool for representing muddy and mixed beds. The
666 cohesive bed framework captures the most important aspects of muddy environment: limitations on erosion caused by
667 increased bed strength with depth in the sediment, and changes toward user-defined equilibrium conditions as deposited (or
668 eroded) beds age. The physical processes of self-compaction and associated changes in porosity and bed strength are not
669 modeled, but the framework of particle-class and bed-layer variables are designed to accommodate a compaction algorithm.
670 The equilibrium profile method implemented here adds little computational expense, but allows the model to represent
671 depth-limited erosion, a key property of many cohesive beds.

672 Modeling stratigraphy effectively is challenging. Although conserving sediment mass among a fixed number of layers is
673 straightforward, it has proven difficult to devise a robust and efficient method that records relevant stratigraphic events in a
674 modeled sediment bed over the wide range of conditions that occur in coastal domains. For both sediment transport and
675 sediment bed geochemistry (i.e. Moriarty et al. 2017; Birchler et al. 2018), it can be important for the sediment bed model to
676 achieve its highest vertical resolution near the sediment – water interface, but the original ROMS sediment bed model did
677 not meet that goal when the sediment bed was subject to frequent or repeated cycles of erosion. The modifications we have

678 made to the bed-layer management have improved the fidelity with which we can record stratigraphic events in the model
679 layers, particularly at the sediment – water interface. Inclusion of biodiffusive mixing is important for environments where
680 biological activity is rapid, compared with sedimentation or physical reworking. Additionally, for problems of sediment
681 geochemistry, it is important to account for mixing of both particulate matter and porewater. Expansion of the ROMS
682 sediment bed model to include diffusive mixing facilitates its use for interdisciplinary problems (i.e. Moriarty et al. 2017;
683 Birchler et al. 2018). The choice of appropriate mixing parameters remains a challenge, especially when considering the
684 spatial and seasonal heterogeneity of biological activity.

685 Overall, the cohesive and mixed-bed algorithms we have introduced in ROMS provide tools that should be useful for both
686 numerical experimentations and realistic applications for fine-grained, and mixed-bed environments. The model applies to
687 dilute suspensions at high Reynolds number (fully turbulent flow) because the turbulence sub-models do not account for
688 particle influences on turbulence dissipation or momentum transfer (e.g., Hsu et al., 2003; Le Hir et al., 2001; Mehta, 1991;
689 2014), so fluid muds and non-Newtonian flows are not represented. We have not quantified the sediment concentrations or
690 range of hydrodynamic parameters for which the model approximations are valid, but a common boundary for fluid mud
691 (where viscoplastic properties become important) is 10 kg/m^3 (Einstein and Krone, 1962; Kirby, 1988). Other processes
692 associated with cohesive or mixed sediment that have not been included are: flow-induced infiltration of fine material into a
693 porous bed (Huettel et al., 1999); changes to the erodibility of mud that has been exposed at low tide (e.g., Paterson et al,
694 1990; Pilditch et al., 2008) or changes to erodibility caused by flora or fauna (e.g., de Boer, 1981; de Deckere et al., 2001;
695 Malarkey et al., 2015; Parsons et al, 2016). It is important to note that the mass settling fluxes of mixed (sand + mud)
696 suspensions may be overestimated if their interactions are not considered, as is the case in the approach taken here (Manning
697 et al., 2010, Manning et al., 2011; Spearman et al., 2011). Nonetheless, our implementation of flocculation, bed
698 consolidation, and bed-mixing modules enhance the utility of the ROMS sediment model for interdisciplinary studies
699 including ecosystem feedbacks (light attenuation, biogeochemistry), and contaminant transport.

700 **6 Conclusion**

701 This paper describes three ways in which the sediment model of Warner et al. (2008) has been enhanced, allowing
702 simulations to be made for non-cohesive, cohesive, and mixed sediment and allowing it to be applied in a wider range of
703 studies. A flocculation model has been added, following Verney et al. (2011). The cohesive bed model developed by Sanford
704 (2008) has been added, allowing the erodibility of the sediment bed to evolve in response to the erosional and depositional
705 history. Mixing between bed layers has been implemented as biodiffusion using a user-specified diffusion coefficient profile.
706 In addition, the sediment bed layering routine has been modified so that bed layers maintain a high resolution near the
707 sediment water interface, as demonstrated by both our idealized and realistic case studies presented here. The paper presents

708 results of model runs that test and demonstrate these new features and to show their application to real-world systems. The
709 authors encourage the coastal modeling community to use, evaluate, and improve upon the new routines.

710 **Code and Data Availability**

711 The algorithms described here have been implemented in ROMS (version 3.6) distributed with the Coupled Ocean
712 Atmosphere Waves Sediment-Transport Modeling System (COAWST, Subversion repository revision number XXXX).
713 COAWST is an open-source community modeling system with a Subversion source-control system maintained by John C.
714 Warner (jcwarner@usgs.gov) and distributed under the MIT/X License (Warner et al., 2010). The COAWST distribution
715 files contain source code derived from ROMS, WRF, SWAN, MCT, and SCRIP, along with Matlab code, examples, and a
716 User's Manual.

717 **Supplement Link (supplied by Copernicus)**

718 **Team List**

719 **Author Contribution**

720 C.R. Sherwood and A. Aretxabaleta shared development of the model code and test cases and most of the manuscript
721 preparation. J.P. Rineheimer was an early user of the cohesive bed model and, along with C.K. Harris, developed the York
722 River application. R. Verney graciously supplied his FORTRAN version of FLOCMOD and helped with adaptation for
723 ROMS. B. Ferré contributed to the early development and application of the model. All authors contributed to the final
724 version.

725 **Competing Interests**

726 The authors declare that they have no conflict of interest.

727 **Disclaimer**

728 Use of firm and product names is for descriptive purposes only and does not imply endorsement by the U.S. Government.

730 **Acknowledgements**

731 The authors thank Jeremy Spearman, Alexis Beudin, Julia Moriarity and five anonymous reviewers (two from *Ocean*
732 *Dynamics* and three from *Geoscientific Model Development*) for helpful comments on earlier drafts of this manuscript. This
733 work was been supported by the U.S. Geological Survey, Coastal and Marine Geology Program and the National Ocean
734 Partnership Program. C.K. Harris was supported by NSF (OCE-1459708, OCE-1061781, and OCE-0536572). This is
735 contribution number XXXX of the Virginia Institute of Marine Sciences. B. Ferré is affiliated with the Centre of Excellence:
736 Arctic Gas hydrate, Environment and Climate (CAGE) funded by the Norwegian Research Council (grant no. 223259). The
737 model code is implemented in ROMS version 3.6, as distributed with the COAWST modeling system (Subversion repository
738 revision 1179; Warner et al., 2010), and is freely available by request to John C. Warner (jcwarnar@usgs.gov) at the U.S.
739 Geological Survey.

740 **References**

- 741 Amoudry, L. O., and Souza, A. J.: Deterministic coastal morphological and sediment transport modeling: a review and
742 discussion, *Rev. Geophys.*, 49 (RG2002), 21, doi:10.1029/2010RG000341, 2011.
- 743 Ariathurai, R., Arulanandan, K., Erosion Rates of Cohesive Soils, *ASCE Journal of the Hydraulics Division* 104, 279–283,
744 1978.
- 745 Booij, N., Ris, R.C., and Holthuijsen, L.H.: A third-generation wave model for coastal regions: 1. Model description and
746 validation. *J. Geophys. Res.* 104, 7649–7666. <https://doi.org/10.1029/98JC02622>, 1999.
- 747 Boudreau B. P.: Is burial velocity a master parameter for bioturbation? *Geochim. Cosmochim. Ac.*, 58, 1243-1250, 1994.
- 748 Boudreau, B. P.: *Diagenetic Models and Their Implementation*, Springer-Verlag, Berlin, 414 pp, 1997.
- 749 Beudin, A., Kalra, T. S., Ganju, N. K., and Warner, J. C.: Development of a Coupled Wave-Flow-Vegetation Interaction
750 Model, *Comput. Geosci.* 100, 76–86, doi:10.1016/j.cageo.2016.12.010, 2017.
- 751 Birchler, J.J., Harris, C. K., Kniskern, T.A., and Sherwood, C.R.: Numerical model of geochronological tracers for
752 deposition and reworking applied to the Mississippi subaqueous delta. *J. of Coast. Res.* in press, 2018.
- 753 Burchard, H. and Baumert, H.: The formation of estuary turbidity maxima due to density effects in the salt wedge. A
754 hydrodynamic process study, *J. Phys. Oceanogr.*, 20, 2, 309–321, 1998.

755 Butman B., Aretxabaleta, A. L., Dickhudt, P. J., Dalyander, P. S., Sherwood, C. R., Anderson, D. M., Keafer, B. A., and
756 Signell, R. P.: Investigating the importance of sediment resuspension in *Alexandrium fundyense* cyst population
757 dynamics in the Gulf of Maine, *Deep-Sea Res. PT II*, 103, 74–95, doi:10.1016/j.dsr2.2013.10.011, 2014.

758 Caldwell, R. L., and Edmonds, D. A.: The effects of sediment properties on deltaic processes and morphologies: A
759 numerical modeling study, *J. Geophys. Res. Earth Surf.*, 119, 961–982, doi:10.1002/2013JF002965, 2014.

760 Cartwright, G.M., C.T. Friedrichs, C.T., and Smith, J. S.: A test of the ADV-based Reynolds-flux method for in situ
761 estimation of sediment settling velocity in a muddy estuary. *Geo-Marine Letters*, 33: 477-484.
762 <http://dx.doi.org/10.1007/s00367-013-0340-4>, 2013.

763 de Boer, P.L.: Mechanical effects of micro-organisms on intertidal bedform migration. *Sedimentology* 28, 129–132.
764 <https://doi.org/10.1111/j.1365-3091.1981.tb01670.x>, 1981.

765 de Deckere, E.M.G.T., Tolhurst, T.J., de Brouwer, J.F.C.: Destabilization of Cohesive Intertidal Sediments by Infauna. *Est.,*
766 *Coast. and Shelf Sci.* 53, 665–669. <https://doi.org/10.1006/ecss.2001.0811>, 2001.

767 del Barrio, P., Ganju, N. K., Aretxabaleta, A. L., Hayn, M., García, A., and Howarth, R. W.: Modeling Future Scenarios of
768 Light Attenuation and Potential Seagrass Success in a Eutrophic Estuary, *Estuar. Coast. Shelf Sci.*, 149, 13–23,
769 doi:10.1016/j.ecss.2014.07.005, 2014.

770 Dickhudt, P. J.: Controls on erodibility in a partially mixed estuary: York River, Virginia, M. S. Thesis, College of William
771 and Mary, Gloucester Point, VA, 2008.

772 Dickhudt, P. J., Friedrichs, C. T., Schaffner, L. C., and Sanford, L. P.: Spatial and temporal variation in cohesive sediment
773 erodibility in the York River estuary, eastern USA: A biologically influenced equilibrium modified by seasonal
774 deposition, *Mar. Geol.*, 267, 3–4, 128–140. doi:10.1016/j.margeo.2009.09.009, 2009.

775 Dickhudt, P. J., Friedrichs, C. T., and Sanford, L. P.: Mud matrix solids fraction and bed erodibility in the York River
776 estuary, USA, and other muddy environments, *Cont. Shelf Res.*, 31, (10, Supplement), S3-S13,
777 doi:10.1016/j.csr.2010.02.008, 2011.

778 DiToro, D. M.: *Sediment Flux Modeling*, Wiley-Interscience, New York, 624 pp, 2001.

779 Ditschke, D. and Markofsky, M.: A time-dependent flocculation model, in: Kusuda, T., Yamanishi, H., Spearman, J.,
780 Gailani, J. Z. (Eds.) *Sediment and Ecohydraulics - INTERCOH 2005, Proceedings in Marine Science*, 9, Elsevier,
781 Amsterdam, 241–253, doi:10.1016/S1568-2692(08)80019-8, 2008.

- 782 Droppo, I. G., Leppard, G. G., Liss, S. N., and Milligan, T. G.: Opportunities, needs, and strategic direction for research on
783 flocculation in natural and engineered systems, in: Droppo, I. G., Leppard, G. G., Liss, S. N., and Milligan, T. G.,
784 (Eds.), *Flocculation in Natural and Engineered Environmental Systems*, CRC Press, London, 407–421, 2005.
- 785 Dyer, K. R.: *Coastal and Estuarine Sediment Dynamics*, John Wiley and Sons, Chichester, 1986.
- 786 Edmonds, D. A., and Slingerland, R. L.: Significant effect of sediment cohesion on delta morphology, *Nat. Geosci.*, 3(2),
787 105–109, doi:10.1038/NGE0730, 2010.
- 788 Eisma, D.: Flocculation and de-flocculation of suspended matter in estuaries, *Neth. J. Sea Res.*, 20, 2/3, 183–199, 1986.
- 789 Einstein H. A., Krone R. B.: Experiments to determine modes of cohesive sediment transport in salt water. *J. Geophys. Res.*
790 67, 1451–1461. <https://doi.org/10.1029/JZ067i004p01451>, 2012.
- 791 Fall, K. A., Harris, C. K., Friedrichs, C. T., Rinehimer, J. P., and Sherwood, C. R.: Model behavior and sensitivity in an
792 application of the cohesive bed component of the Community Sediment Transport Modeling System for the York
793 River Estuary, VA, USA, *J. Mar. Sci. Eng.*, 2, 413–436, doi:10.3390/jmse2020413, 2014.
- 794 Fasham, M. J. R., Ducklow, H. W., and McKelvie S. M.: A nitrogen-based model of plankton dynamics in the oceanic
795 mixed layer, *J. Mar. Res.*, 48, 591-639, 1990.
- 796 Fennel, K., Wilkin, J., Levin, J., Moisan, J., and O'Reilly, J.: Nitrogen cycling in the Middle Atlantic Bight: Results from a
797 three-dimensional model and implications for the North Atlantic nitrogen budget, *Global Biogeochem. Cycles*, 20,
798 GB3007, 14, 2006.
- 799 Harris, C. K. and Wiberg, P. L.: Approaches to quantifying long-term continental shelf sediment transport with an example
800 from the northern California STRESS mid-shelf site, *Cont. Shelf Res.*, 17, 1389–1418, 1997.
- 801 Harris, C. K. and Wiberg, P. L.: A two-dimensional, time-dependent model of suspended sediment transport and bed
802 reworking for continental shelves, *Comput. Geosci.*, 27, 6, 675–690, 2001.
- 803 Hill, P. S.: Sectional and discrete representations of floc breakage in agitated suspensions, *Deep-Sea Res. PT I*, 43, 5, 679–
804 702, 1996.
- 805 Hill, P. S. and Nowell, A. R. M.: Comparison of two models of aggregation in continental-shelf bottom boundary layers, *J.*
806 *Geophys. Res.*, 100, C11, 22,749–22,763, 1995.
- 807 Hirano, M.: River bed degradation with armouring, in: *Proceedings, Japan Society of Civil Engineers*, Vol. 195, Japan, 1971.

808 Hsu T.-J., Jenkins, J. T., Liu, P. L.-F.: On two-phase sediment transport: Dilute flow. *Journal of Geophysical Research:*
809 *Oceans* 108. <https://doi.org/10.1029/2001JC001276>, 2003.

810 Huettel, M., Ziebis, W., Forster, S.: Flow-induced uptake of particulate matter in permeable sediments. *Limnol. Oceanogr.*
811 41, 309–322. <https://doi.org/10.4319/lo.1996.41.2.0309>, 1999.

812 HydroQual, Inc.: *A Primer for ECOMSED Version 1.4 Users Manual*, HydroQual, Inc., Mahwah, NJ, 2004.

813 Jacobs, W., Le Hir, P., Van Kesteren, W., and Cann, P.: Erosion threshold of sand - mud mixtures, *Cont. Shelf Res.*, 31, 10
814 Supplement, S14–S25, doi:10.1016/j.csr.2010.05.012, 2011.

815 Keyvani, A. and Strom, K.: Influence of Cycles of High and Low Turbulent Shear on the Growth Rate and Equilibrium Size
816 of Mud Flocs, *Mar. Geol.*, 354, 1–14, doi:10.1016/j.margeo.2014.04.010, 2014.

817 Khelifa, A. and Hill, P. S.: Models for effective density and settling velocity of flocs. *J. Hydraul. Res.*, 44, 3, 390–401, 2006.

818 Kirby, R.: High Concentration Suspension (Fluid Mud) Layers in Estuaries, in: *Physical Processes in Estuaries*. Springer,
819 Berlin, Heidelberg, pp. 463–487. https://doi.org/10.1007/978-3-642-73691-9_23, 1988.

820 Knoch, D. and Malcherek, A.: A numerical model for simulation of fluid mud with different rheological behaviors, *Ocean*
821 *Dyn.*, 61, 245–256, doi: 10.1007/s10236-010-0327-x, 2011.

822 Kranenburg, C.: The fractal structure of cohesive sediment aggregates, *Estuar. Coast. Shelf Sci.*, 39, 451–460, 1994.

823 Krone, R. B.: Flume studies of the transport of sediment in estuarial shoaling processes, Final Report, Hydraulic Engineering
824 Laboratory and Sanitary Engineering Research Laboratory, Univ. of California, Berkeley, 1962.

825 Krone, R. B.: A study of rheologic properties of estuarial sediments, Technical Bulletin 7, Vicksburg, MS., U.S. Army Corps
826 of Engineers Communication on Tidal Hydrodynamics, 1963.

827 Le Hir, P., Bassoullet, P., Jestin, H.: Application of the continuous modeling concept to simulate high-concentration
828 suspended sediment in a macrotidal estuary, in: McAnally, W.H., Mehta, A.J. (Eds.), *Proceedings in Marine*
829 *Science, Coastal and Estuarine Fine Sediment Processes*. Elsevier, pp. 229–247. [https://doi.org/10.1016/S1568-](https://doi.org/10.1016/S1568-2692(00)80124-2)
830 [2692\(00\)80124-2](https://doi.org/10.1016/S1568-2692(00)80124-2), 2000.

831 Le Hir, P., Cayocca, F., and Waeles, B.: Dynamics of sand and mud mixtures: A multiprocess-based modelling strategy,
832 *Cont. Shelf Res.*, 3, 10 Supplement, S135–S149, 2011.

- 833 Lecroart, P., Maire, O., Schmidt, S., Grémare, A., Anschutz, P., and Meysman F. J. R.: Bioturbation, short-lived
834 radioisotopes, and the tracer-dependence of biodiffusion coefficients, *Geochim. Cosmochim. Ac.*, 74, 21, 6049–
835 6063, doi:10.1016/j.gca.2010.06.010, 2010.
- 836 Letter, J. V.: Significance of probabilistic parameterization in cohesive sediment bed exchange, Ph.D. Thesis, Univ. of
837 Florida, Gainesville, 2009.
- 838 Letter, J. V. and Mehta, A. J.: A heuristic examination of cohesive sediment bed exchange in turbulent flows, *Coast. Eng.*,
839 58, 779–789, 2011.
- 840 Li, Q. W., Benson M. Harlan, M., Robichaux, P., Sha, X., Xu, K., and Straub, K. M.: Influence of sediment cohesion on
841 deltaic morphodynamics and stratigraphy over basin-filling time scales. *J. Geophys. Res. Earth Surf.* 2017JF004216
842 doi:10.1002/2017JF004216, 2017.
- 843 Lick, W., Huang, H., and Jepsen, R.: Flocculation of fine-grained sediment due to differential settling, *J. Geophys. Res.*, 98,
844 10279–10288, 1993.
- 845 Lumborg, U. and Windelin, A.: Hydrography and cohesive sediment modelling: application to the Romo Dyb tidal area, *J.*
846 *Mar. Syst.*, 38, 3-4, 287–303, 2003.
- 847 Lumborg, U.: Modelling the deposition, erosion, and flux of cohesive sediment through Oresund, *J. Mar. Syst.*, 56, 1-2,
848 179–193, 2005.
- 849 Lumborg, U. and Pejrup, M.: Modelling of cohesive sediment transport in a tidal lagoon--an annual budget, *Mar. Geol.*, 218,
850 1-4, 1–16, 2005.
- 851 Maa, J. P.-Y., Sanford, L. P. and Schoellhamer, D. H. (Eds): *Estuarine and Coastal Fine Sediment Dynamics: INTERCOH*
852 2003, vol 8, *Proceedings in Marine Science*, Elsevier, Amsterdam, 2007.
- 853 MacCready, P., and Geyer, W. R.: Estuarine salt flux through an isohaline surface, *J. Geophys. Res.*, 106, 11629–11637,
854 2001.
- 855 MacDonald, I., Vincent, C. E., Thorne, P. D., and Moate, B. D.: Acoustic scattering from a suspension of flocculated
856 sediments, *J. Geophys. Res.*, 118, 2581–2594, doi:10.1002/jgrc.20197, 2013.
- 857 Maerz, J., Verney, R., Wirtz, K., Feudel, U.: Modeling flocculation processes: Intercomparison of a size class-based model
858 and a distribution-based model. *Cont. Shelf Res.*, *Proceedings of the 9th International Conference on Nearshore and*
859 *Estuarine Cohesive Sediment Transport Processes* 31, S84–S93. <https://doi.org/10.1016/j.csr.2010.05.011>, 2011.

- 860 Malarkey, J., Baas, J.H., Hope, J.A., Aspden, R.J., Parsons, D.R., Peakall, J., Paterson, D.M., Schindler, R.J., Ye, L.,
861 Lichtman, I.D., Bass, S.J., Davies, A.G., Manning, A.J., Thorne, P.D.: The pervasive role of biological cohesion in
862 bedform development. *Nature Communications* 6, 6257. <https://doi.org/10.1038/ncomms7257>, 2015.
- 863 Manning, A.J., Baugh, J.V., Spearman, J.R., Whitehouse, R.J.S.: Flocculation settling characteristics of mud: sand mixtures.
864 *Ocean Dynamics* 60(2), 237–253. <https://doi.org/10.1007/s10236-009-0251-0>, 2010.
- 865 Manning, A.J., Baugh, J.V., Spearman, J.R., Pidduck, E.L., Whitehouse, R.J.S.: The settling dynamics of flocculating mud-
866 sand mixtures: Part 1—Empirical algorithm development. *Ocean Dynamics* 61(2-3), 311–350.
867 <https://doi.org/10.1007/s10236-011-0394-7>, 2011.
- 868 Manning, A. J., Dyer, K. R.: Mass settling flux of fine sediments in Northern European estuaries: measurements and
869 predictions. *Marine Geology* 245, 107–122, 2007.
- 870 McAnally, W. H.: *Aggregation and Deposition of Estuarial Fine Sediment*, Ph.D. Thesis, Univ. of Florida, 382 pp, 1999.
- 871 McAnally, W. H. and Mehta, A. J.: Collisional aggregation of fine estuarial sediment, in: McAnally, W. H. and Mehta, A. J.
872 (Eds.), *Coastal and Estuarine Fine Sediment Processes*, Elsevier, 19-39, 2001.
- 873 McCave, I. N. and Swift, S. A.: A physical model for the deposition of fine-grained sediments in the deep sea, *Bull. Geol.*
874 *Soc. Am.*, 87, 541–546, 1976.
- 875 McCave, I. N.: Size spectra and aggregation of suspended particles in the deep ocean, *Deep-Sea Res.*, 31, 4, 329–352, 1984.
- 876 Mehta, A. J.: Characterization of cohesive sediment properties and transport processes in estuaries, in: Mehta, A. J. (Ed.)
877 *Lecture Notes on Coastal and Estuarine Studies*, Vol 14, Springer, Berlin, 290–325, 1986.
- 878 Mehta, A.J.: Understanding fluid mud in a dynamic environment. *Geo-Marine Letters* 11, 113–118.
879 <https://doi.org/10.1007/BF02430995>, 1991.
- 880 Mehta, A. J.: *An Introduction to the Hydraulics of Fine Sediment Transport*, World Scientific, 1039 pp, 2014.
- 881 Mengual, B., Hir, P.L., Cayocca, F., Garlan, T. : *Modelling Fine Sediment Dynamics: Towards a Common Erosion Law for*
882 *Fine Sand, Mud and Mixtures*. *Water* 9(8), 564. <https://doi.org/10.3390/w9080564>, 2017.
- 883 Merkel, U. H. and Kopmann, R.: A continuous vertical grain sorting model for Telemac & Sisyphe, in: Munoz, R. M. (Ed)
884 *River Flow 2012*, Taylor & Francis, London, 2012.

885 Michalakes, J., Chen, S., Dudhia, J., Hart, L., Klemp, J., Middlecoff, J., and Skamarock, W.: Development of a next-
886 generation regional weather research and forecast model, in: *Developments in Teracomputing*. World Scientific, pp.
887 269–276. https://doi.org/10.1142/9789812799685_0024, 2001.

888 Mietta, F., Chassagne, C., Manning, A.J., Winterwerp, J.C.: Influence of shear rate, organic matter content, pH and salinity
889 on mud flocculation. *Ocean Dynamics* 59, 751–763. <https://doi.org/10.1007/s10236-009-0231-4>, 2009.

890 Mitchener, H. and Torfs, H.: Erosion of mud/sand mixtures, *Coast. Eng.*, 29, 1-2, 1–25, 1996.

891 Moriarty, J.M., Harris, C.K., Fennel, K., Friedrichs, M.A.M., Xu, K., and Rabouille, C.: The roles of resuspension, diffusion
892 and biogeochemical processes on oxygen dynamics offshore of the Rhône River, France: a numerical modeling
893 study. *Biogeosciences* 14, 1919-1946, 2017.

894 Nguyen, H.-H. and Chua, L. H. C.: Simplified physically based model for estimating effective floc density, *J. Hydraul. Eng.*,
895 137, 8, 843–846, 2011.

896 Panagiotopoulos, I., Voulgaris, G., and Collins, M. B.: The influence of clay on the threshold of movement in fine sandy
897 beds, *Coast. Eng.*, 32, 19–43, 1997.

898 Parsons, D. R., Schindler, R. J., Hope, J. A., Malarkey, J., Baas, J. H., Peakall, J., Manning, A. J., Ye, L., Simmons, S.,
899 Paterson D. M., Aspden, R. J., Bass, S. J., Davies, A. G., Lichtman, I. D., Thorne, P. D.: The role of biophysical
900 cohesion on subaqueous bed form size. *Geophys. Res. Letters* 43(4), 1566–1573.
901 <https://doi.org/10.1002/2016GL067667>, 2016.

902 Paterson, D.M., Crawford, R.M., Little, C.: Subaerial exposure and changes in the stability of intertidal estuarine sediments.
903 *Est., Coast. and Shelf Sci.* 30, 541–556. [https://doi.org/10.1016/0272-7714\(90\)90091-5](https://doi.org/10.1016/0272-7714(90)90091-5), 1990.

904 Pilditch, C.A., Widdows, J., Kuhn, N.J., Pope, N.D., Brinsley, M.D.: Effects of low tide rainfall on the erodibility of
905 intertidal cohesive sediments. *Cont. Shelf Res.* 28, 1854–1865. <https://doi.org/10.1016/j.csr.2008.05.001>, 2008.

906 Ralston, D. K., Geyer, W. R. and Warner, J. C.: Bathymetric controls on sediment transport in the Hudson River estuary:
907 Lateral asymmetry and frontal trapping, *J. Geophys. Res.* 117, C10013, 2012.

908 Rinehimer, J. P., Harris, C. K., Sherwood, C. R., and Sanford, L. P.: Sediment consolidation in a muddy, tidally-dominated
909 environment: Model behavior and sensitivity, *Estuarine and Coastal Modeling*, Proceedings of the Tenth
910 International Conference: 819–838, 2008.

911 Sanford, L. P. and Maa, J. P. Y.: A unified erosion formulation for fine sediments, *Mar. Geol.*, 179(1-2), 9–23, 2001.

- 912 Sanford, L. P.: Modeling a dynamically varying mixed sediment bed with erosion, deposition, bioturbation, consolidation,
913 and armoring, *Comput. Geosci.*, 34(10), 1263–1283, 2008.
- 914 Shchepetkin, A. F. and McWilliams, J. C.: The Regional Oceanic Modeling System (ROMS): A Split-Explicit, Free-Surface,
915 Topography-Following-Coordinate Oceanic Model, *Ocean Model.*, 9, 4, 347–404,
916 doi:10.1016/j.ocemod.2004.08.002, 2005.
- 917 Sherwood, C. R., Drake, D. E., Wiberg, P. L., and Wheatcroft, R. A.: Prediction of the fate of p,p'-DDE in sediment on the
918 Palos Verdes shelf, California, USA, *Cont. Shelf Res.*, 22, 6-7, 1025–1058, 2002.
- 919 Slade, W. H., Boss, E. S., and Russo, C.: Effects of particle aggregation and disaggregation on their inherent optical
920 properties, *Opt. Express*, 19, 9, 7945–7959, 2011.
- 921 Smoluchowski, M.: Versuch einer mathematischen theorie des koagulations-kinetik kolloid losungren, *Zeitschrift fur*
922 *Physikalische Chemie*, 92, 129–168, 1917.
- 923 Soulsby, R. L., Manning, A. J., Spearman, J., and Whitehouse, R. J. S.: Settling Velocity and Mass Settling Flux of
924 Flocculated Estuarine Sediments, *Mar. Geol.*, 339, 1–12, doi:10.1016/j.margeo.2013.04.006, 2013.
- 925 Spearman, J. R., Manning, A. J., and Whitehouse, R. J. S.: The settling dynamics of flocculating mud and sand mixtures:
926 part 2—numerical modelling. *Ocean Dyn.*, 61, 351–370, 2011.
- 927 Spearman, J., Manning, A.J.: On the significance of mud transport algorithms for the modelling of intertidal flats, in:
928 Kusuda, T., Yamanishi, H., Spearman, J., Gailani, J.Z. (Eds.), Chapter 28 in: *Proceedings in Marine Science,*
929 *Sediment and Ecohydraulics.* Elsevier, pp. 411–430. [https://doi.org/10.1016/S1568-2692\(08\)80030-7](https://doi.org/10.1016/S1568-2692(08)80030-7), 2008.
- 930 Stone, M., Krishnappan, B. G., and Emelko, M. B.; The effect of bed age and shear stress on the particle morphology of
931 eroded cohesive river sediment in an annular flume, *Water Res.*, 42, 15, 4179–4187, doi:
932 10.1016/j.watres.2008.06.019, 2008.
- 933 Swift, D. J. P., Stull, J. K., Niedoroda, A. W., Reed, C. W., Wong, G. T. F., and Foyle, B. A.: Estimates of the Biodiffusion
934 Coefficient, DB, from Composition of the Benthic Infaunal Community, Report prepared for the Los Angeles
935 County Sanitation Districts, Contribution No. 5 of the Sediment Dynamics Laboratory, Old Dominion University,
936 Norfolk, Virginia, 1994.
- 937 Swift, D. J. P., Stull, J. K., Niedoroda, A. W., Reed, C. W., and Wong, G. T. F.: Contaminant dispersal on the Palos Verdes
938 continental margin: II. Estimates of biodiffusion coefficient, Db, from composition of the benthic infaunal
939 community, *Sci. Total Environ.*, 179, 91–107, 1996.

- 940 Tambo, N. and Watanabe, Y.: Physical characteristics of flocs. I The floc density function and aluminium floc. *Water*
941 *Research* 13, 409–419, 1979.
- 942 Tassi, P. and Villaret, C.: SISYPHE v6.3 User's Manual, EDF, Laboratoire National d'Hydraulique et Environnement,
943 Chatou, France, 73 pp, 2014.
- 944 Thorne, P. D., MacDonald, I. T., and Vincent, C. E.: Modelling acoustic scattering by suspended flocculating sediments,
945 *Cont. Shelf Res.*, 88, 81–91, doi:10.1016/j.csr.2014.07003, 2014.
- 946 Tolman, H.L. and the WAVEWATCH III Development Group: User manual and system documentation of WAVEWATCH
947 III version 4.18, Technical Note. Environmental Modeling Center, National Centers for Environmental Prediction,
948 National Weather Service, National Oceanic and Atmospheric Administration, U.S. Department of Commerce,
949 College Park, MD, 2014.
- 950 Umlauf, L. and Burchard, H.: A generic length-scale equation for geophysical turbulence models, *J. Mar. Res.*, 61, 2, 235–
951 265, 2002.
- 952 van Leussen, W.: Estuarine macroflocs and their role in fine-grained sediment transport, Ph.D. Thesis, University of Utrecht,
953 Utrecht, The Netherlands, 1994.
- 954 van Leussen, W.: Aggregation of Particles, Settling Velocity of Mud Flocs A Review, in: *Physical Processes in Estuaries*.
955 Springer, Berlin, Heidelberg, pp. 347–403. https://doi.org/10.1007/978-3-642-73691-9_19, 1988.
- 956 van Ledden, M., van Kesteren, W. G. M., and Winterwerp, J. C.: A conceptual framework for the erosion behaviour of sand
957 - mud mixtures, *Cont. Shelf Res.*, 24, 1, 1–11. doi:10.1016/j.csr.2003.09.002, 2004.
- 958 van der Wegen, M., Dastgheib, A., Jaffe, B. E., and Roelvink, D.: Bed composition generation for morphodynamic
959 modeling: case study of San Pablo Bay in California, USA, *Ocean Dyn.*, 61, 173–186, doi:10.1007/s10236-010-
960 0314-2, 2011.
- 961 Verney, R., Lafite, R., Brun-Cottan, J. C., and Le Hir, P.: Behaviour of a floc population during a tidal cycle: Laboratory
962 experiments and numerical modeling, *Cont. Shelf Res.*, 31, S64–S83, doi:10.1016/j.csr.2010.02.005, 2011.
- 963 Villaret, C., Hervouet, J.-M., Kopmann, R., Merkel, U., and Davies, A. G.: Morphodynamic modeling using the Telemac
964 finite-element system, *Comput. Geosci.*, 53, 105–113, doi:10.1016/j.cageo.2011.10.004, 2011.
- 965 Warner, J. C., Armstrong, B., He, R., and Zambon, J. B.: Development of a coupled ocean-atmosphere-wave-sediment
966 transport (COAWST) modeling system, *Ocean Model.*, 35, 230–244, doi:10.1016/j.ocemod.2010.07.010, 2010.

967 Warner, J. C., Sherwood, C. R., Arango, H. G., and Signell, R. P.: Performance of four turbulence closure models
968 implemented using a generic length scale method, *Ocean Model.*, 8, 1/2, 81–113, doi:10.1029/2004JC002691,
969 2005.

970 Warner, J. C., Sherwood, C. R., Signell, R. P., Harris, C. K., and Arango, H. G.: Development of a three-dimensional,
971 regional, coupled wave, current, and sediment-transport model, *Comput. Geosci.*, 34, 1284–1306, 2008.

972 Wheatcroft, R. A. and Martin, W. R.: Spatial variation in short-term (^{234}Th) sediment bioturbation intensity along an organic-
973 carbon gradient, *J. Mar. Res.*, 54, 763–792, 1996.

974 Whitehouse, R. J. S., Soulsby, R. L., Roberts, W., and Mitchener, H.: *Dynamics of Marine Muds*, Thomas Telford, London,
975 2000.

976 Wiberg, P. L., Drake, D. E., and Cacchione, D. A.: Sediment resuspension and bed armoring during high bottom stress
977 events on the northern California inner continental shelf: measurements and predictions, *Cont. Shelf Res.*, 14, 10/11,
978 1191–1219, 1994.

979 Winterwerp, J. C.: *On the Dynamics of High-Concentrated Mud Suspensions*, Technical University of Delft, Delft, The
980 Netherlands, 1999.

981 Winterwerp, J. C.: On the flocculation and settling velocity of estuarine mud, *Cont. Shelf Res.*, 22, 9, 1339–1360, 2002.

982 Winterwerp, J. C., Bale, A. J., Christie, M. C., Dyer, K. R., Jones, S., Lintern, D. G., Manning, A. J., Roberts, W., and
983 Kranenburg, C.: Flocculation and settling velocity of fine sediment. In: *Proceedings in Marine Science*, Vol. 5,
984 Elsevier, 25–40, 2002

985 Winterwerp, J. C. and Kranenburg, C. (Eds.): *Fine Sediment Dynamics in the Marine Environment*, *Proceedings in Marine*
986 *Science*, Vol 5, Elsevier, Amsterdam, 2002.

987 Winterwerp, J. C., Maa, J. P.-Y., Sanford, L. P., and Schoellhamer, D. H.: On the sedimentation rate of cohesive sediment,
988 in: *Proceedings in Marine Science*, 8, Elsevier, 209–226, 2007

989 Winterwerp, J. C., Manning, A. J., Martens, C., de Mulder, T., and Vanlede J.: A heuristic formula for turbulence-induced
990 flocculation of cohesive sediment, *Estuar. Coast. Shelf Sci.*, 68, 1-2, 195–207, 2006.

991 Winterwerp, J. C. and van Kesteren, W. G. M.: *Introduction to the Physics of Cohesive Sediment in the Marine*
992 *Environment*, Elsevier, Amsterdam, 2004.

- 993 Xu, F., Wang, D.-P., and Riemer, N.: Modeling flocculation processes of fine-grained particles using a size-resolved
994 method: Comparison with published laboratory experiments, *Cont. Shelf Res.*, 28, 2668–2677.
995 doi:10.1016/j.csr.2008.09.001, 2008.
- 996 Xu, F., Wang, D.-P., and Riemer, N.: An idealized model study of flocculation on sediment trapping in an estuary turbidity
997 maximum, *Cont. Shelf Res.*, 30, 1314–1323. doi:10.1016/j.csr.2010.04.014, 2010.
- 998
- 999

Table 1. Characteristics of the estuary turbidity maxima for seven cases under different flocculation conditions.

Case	0	1	2	3	4	5	6
	No flocs	$\alpha = 0.35$ $\beta = 0.15$ no floc evol.	$\alpha = 0.35$ $\beta = 0.15$ floc evol., 5 h	$\alpha = 0.35$ $\beta = 0.15$ floc evol., 50 h	$\alpha = 0.45$ $\beta = 0.10$ floc evol., 50 h	$\alpha = 0.25$ $\beta = 0.20$ floc evol., 50 h	$\alpha = 0.35$ $\beta = 0.34$ floc evol., 50 h
Mean SSC @ maximum (kg/m ³)	1.23	0.46	0.45	0.45	0.45	0.46	0.46
Maximum SSC (kg/m ³)	3.1	3.6	3.7	3.7	4.1	3.2	2.9
D_{50} at SSC maximum (μm)	37	539	529	529	622	426	384
D_{50} at SSC maximum; 12-h mean (μm)	37	255	249	250	325	181	167
w_s at SSC maximum (mm/s)	0.13	1.91	1.87	1.87	2.2	1.51	1.36
w_s at SSC maximum; 12-h mean (mm/s)	0.13	0.90	0.88	0.89	1.15	0.64	0.59
Locus of maximum deposition (km from ocean boundary)	80 ± 30	19 ± 11	18 ± 10	18 ± 11	19 ± 10	79 ± 69	16 ± 6
Maximum deposit thickness (mm)	4.2 ± 5.8	31.6 ± 12.8	25.8 ± 10.1	26.1 ± 10.4	27.1 ± 10.9	5 ± 10.1	25 ± 10.2
Maximum deposit D_{50} (μm)	18.5 ± 0	218 ± 87.1	40.9 ± 71.3	75.5 ± 76.1	92.9 ± 94.2	69.5 ± 89.9	25.4 ± 40.4

1003

1004 **Figures**

1005

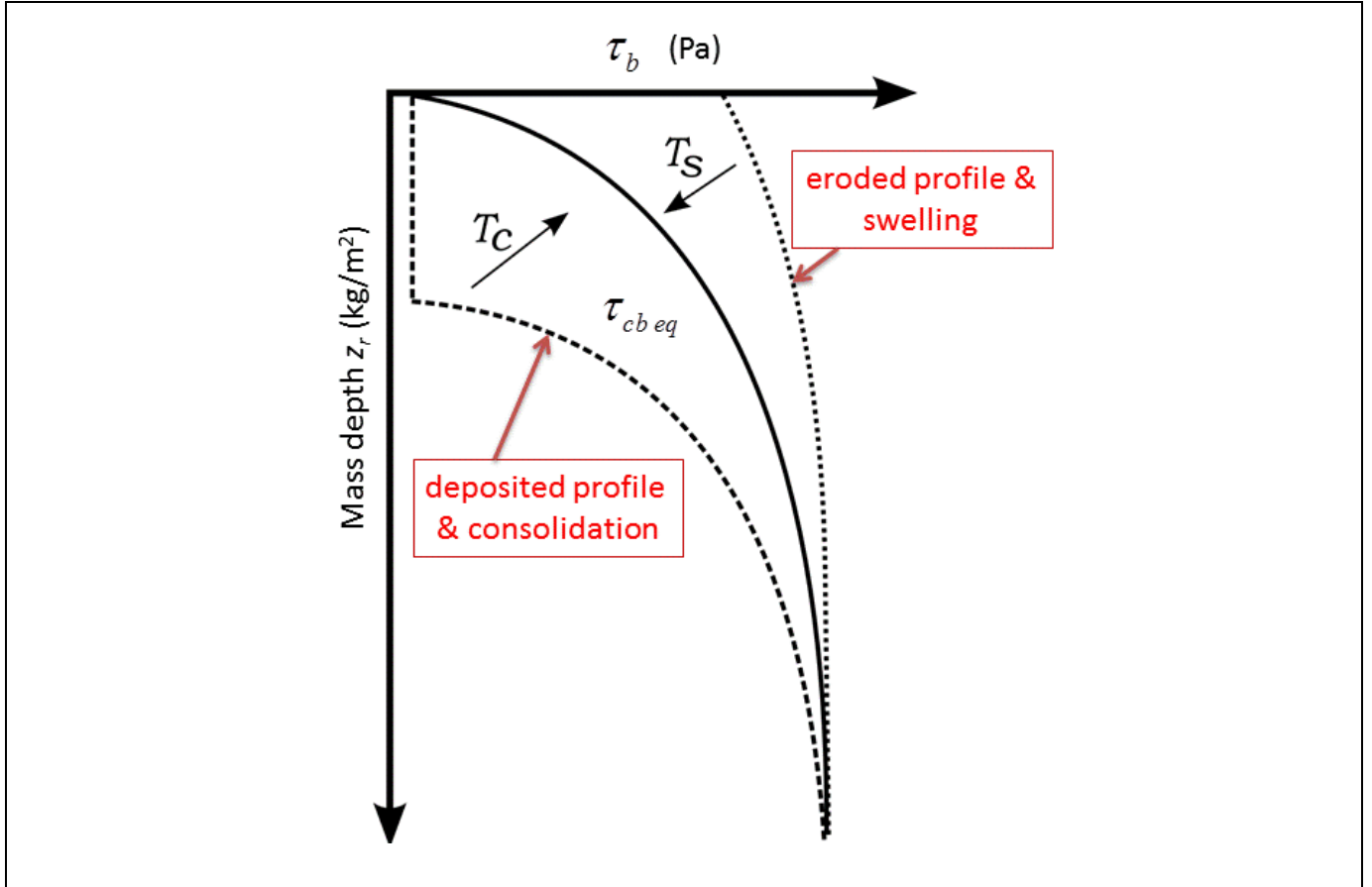


Figure 1. Conceptual diagram of consolidation and swelling (Rinehimer et al., 2008). The equilibrium bulk critical stress for erosion profile, $\tau_{cb eq}(z)$ is shown as the solid line. The dotted line represents a critical shear stress profile following sediment erosion. The dashed line is a profile after deposition of sediment with a low τ_c at the surface. The arrows indicate consolidation and swelling toward the equilibrium profile with the timescales T_c and T_s , respectively.

1006

1007

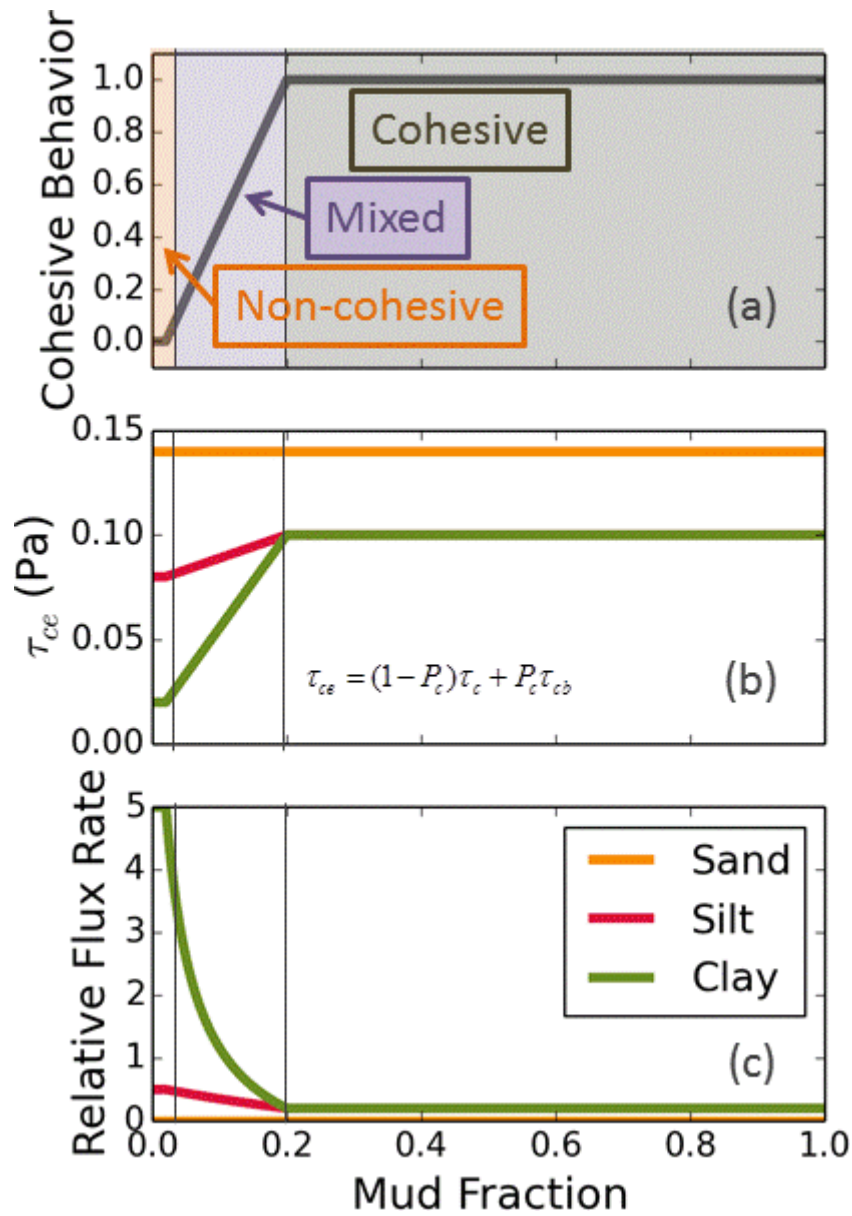


Figure 2. Summary of mixed-bed behavior with increasing of mud fraction f_c (the combined mass fraction of material in cohesive classes). (a) Cohesive behavior parameter P_c as a function of f_c . (b) Effective critical shear stress τ_{ce} for size classes where bulk critical shear stress of the bed $\tau_{cb} = 0.1$ Pa. (c) Relative flux (normalized excess shear stress) from the bed when bed stresses are $\sim \tau_b = 0.12$ Pa (greater than τ_c for clay and silt primary particles, but less than τ_c for sand)

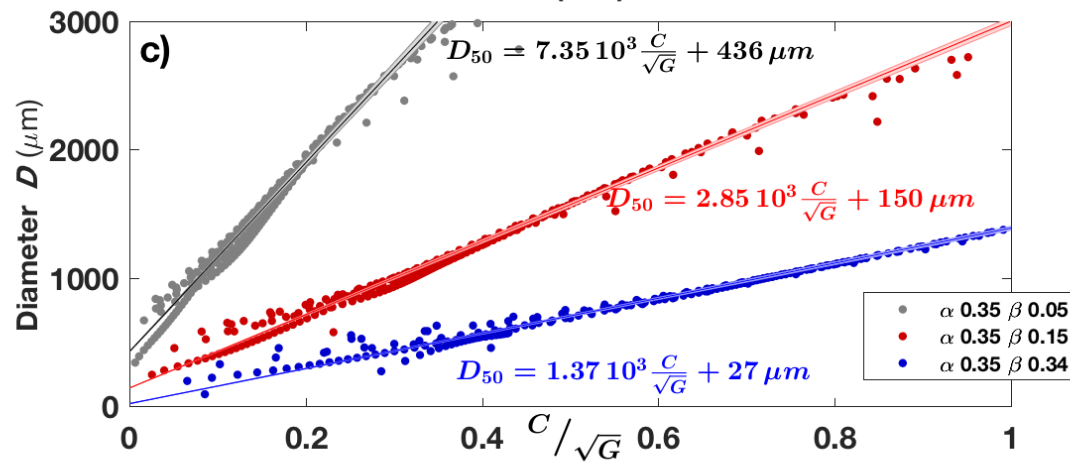
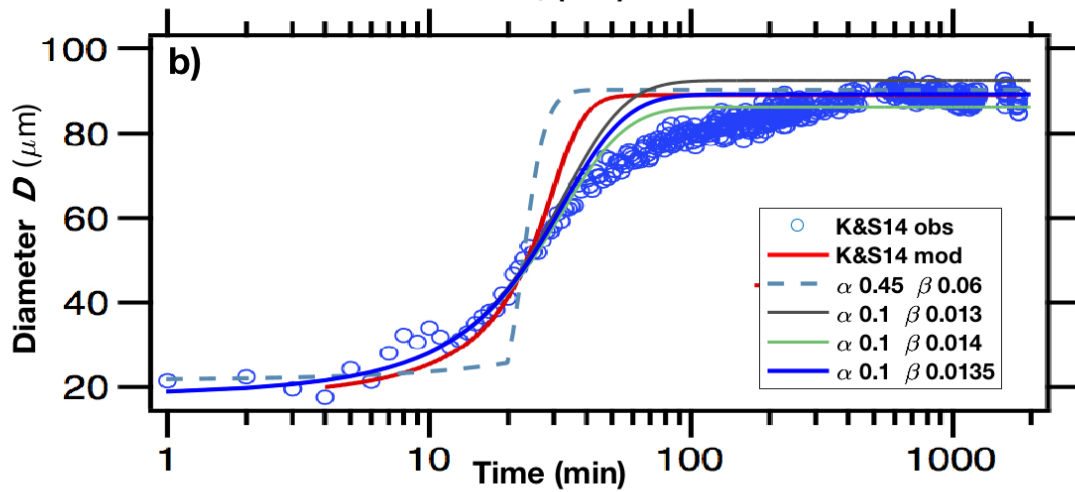
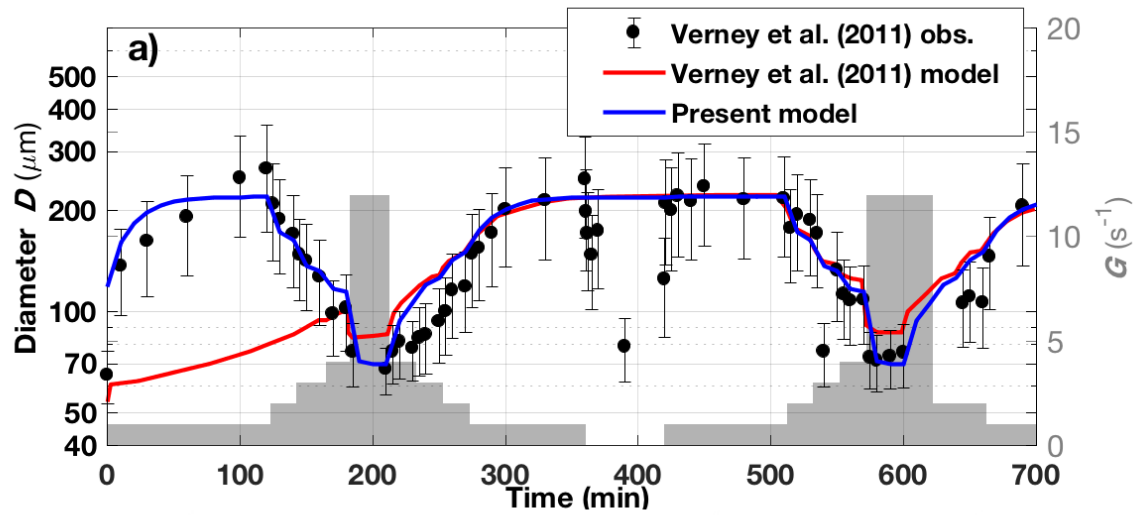


Figure 3. Comparison of ROMS implementation of FLOCMOD with laboratory and theoretical results. (a) Laboratory response of floc size to simulated fluctuations in shear rate G (gray shading) showing observed area-weighted mean floc diameter D (black dots with +/- one standard deviation bars), model results presented in Verney et al., (2011; red line), and ROMS FLOCMOD simulation (blue line). (b) Laboratory response of floc size to rapid increase in shear rate from $G=0$ to $G=15 \text{ s}^{-1}$ showing sizes measured by Keyvani and Strom (2014; K&S14; blue circles), K&S14 model results (red line), and ROMS FLOCMOD results for various combinations of aggregation and breakup parameters (dashed and colored lines). (c) Equilibrium diameters produced by steady ROMS FLOCMOD simulations with a range of concentrations, shear rates, and aggregation and breakup parameters (dots). These fall along lines with slopes determined by the ratio of aggregation and breakup parameters, according to theory (Winterwerp, 1998).

1008

1009

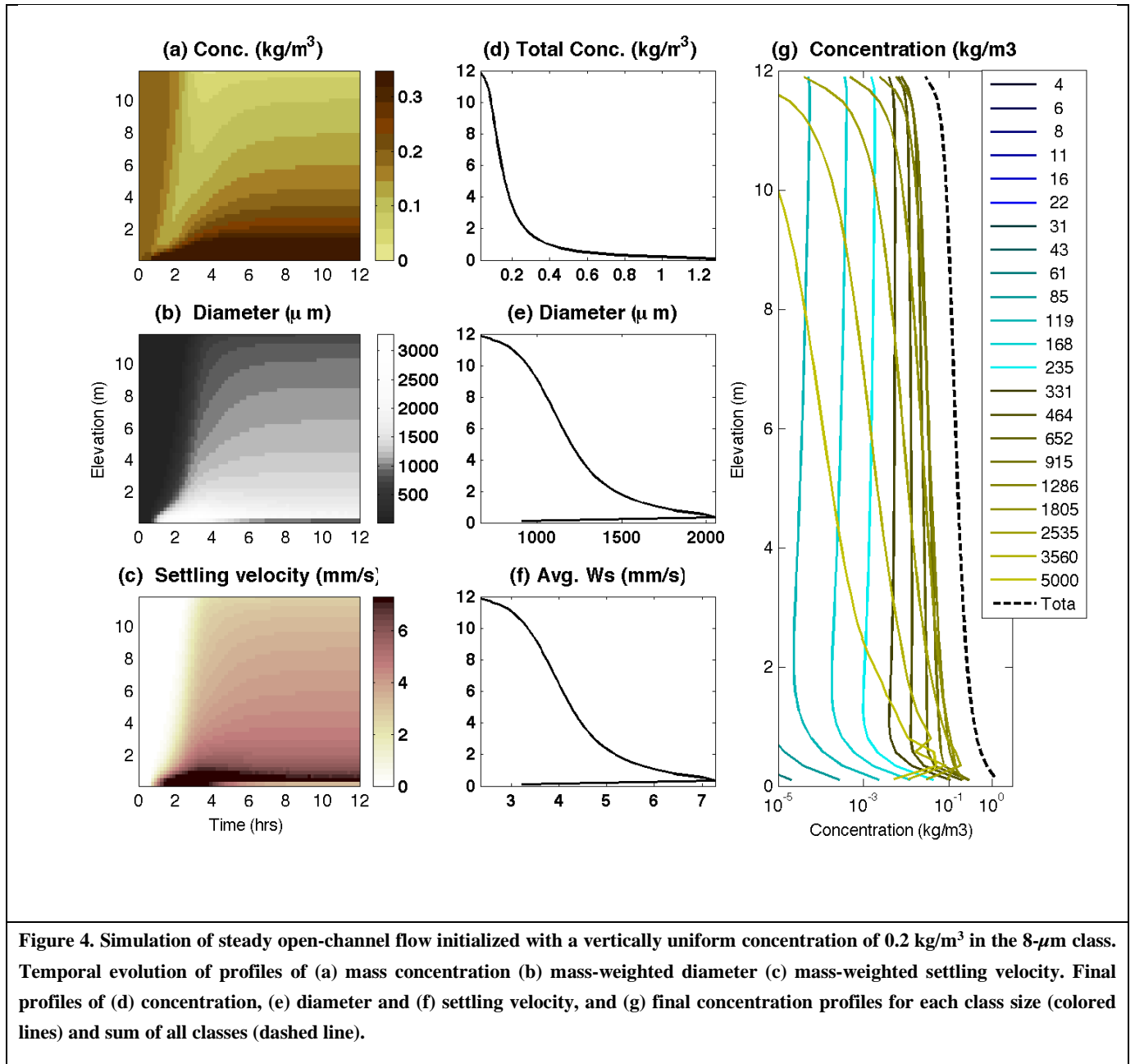


Figure 4. Simulation of steady open-channel flow initialized with a vertically uniform concentration of 0.2 kg/m³ in the 8-μm class. Temporal evolution of profiles of (a) mass concentration (b) mass-weighted diameter (c) mass-weighted settling velocity. Final profiles of (d) concentration, (e) diameter and (f) settling velocity, and (g) final concentration profiles for each class size (colored lines) and sum of all classes (dashed line).

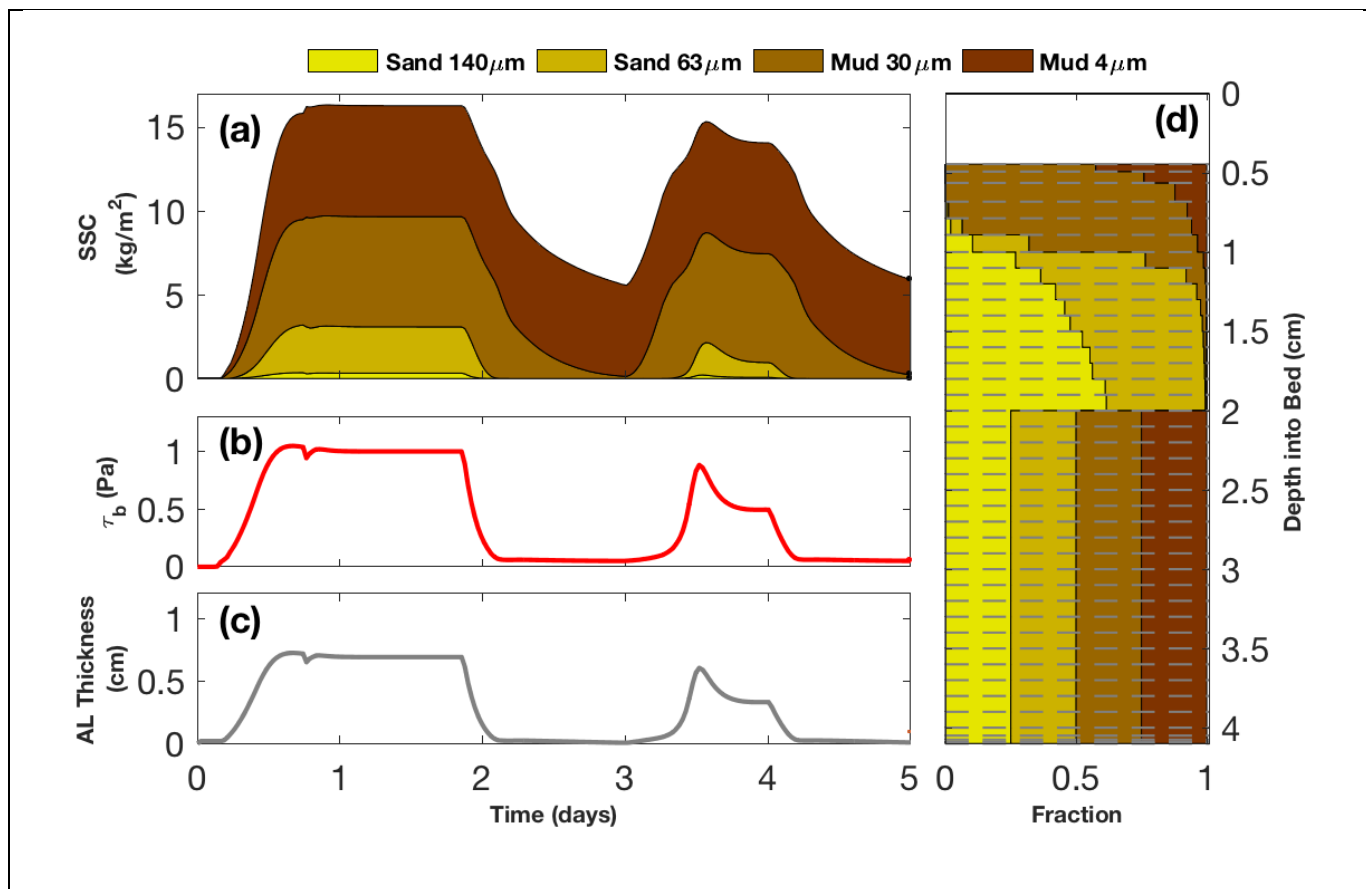


Figure 5. Summary of the double resuspension experiment with non-cohesive sediment over 5 days. The model setup included 41 bed layers, a minimum new layer thickness of 1 mm, and four non-cohesive classes. The top horizontal panel (a) shows the time evolution of the mass of sediment in suspension, colored by size class. The middle horizontal panel (b) is the time series of bottom stress, and the bottom horizontal panel (c) shows the corresponding time series of active-layer thickness. The right panel (d) depicts the final stratigraphy relative to the initial bed level at zero and shows the fraction of each sediment class in each bed layer.

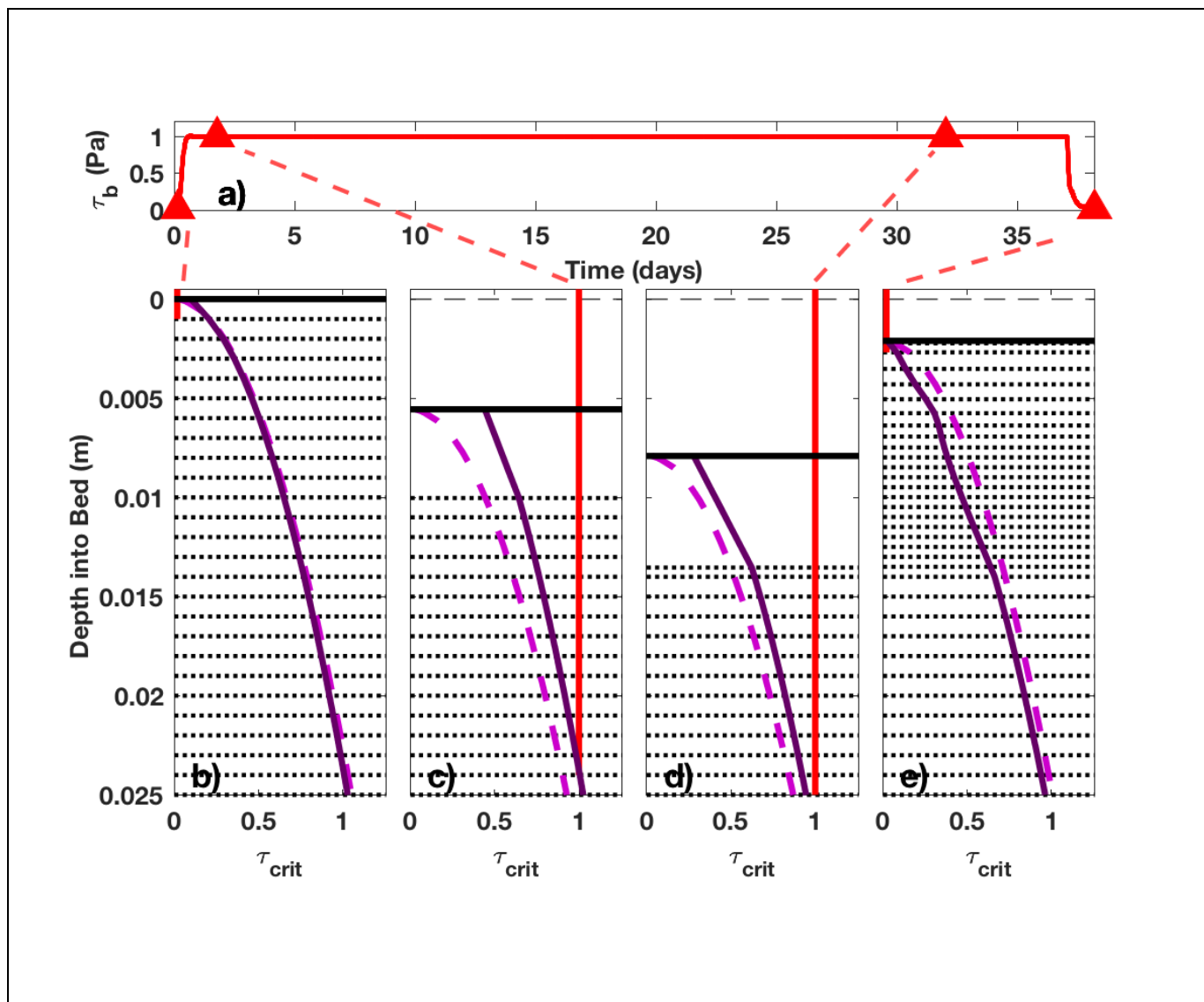
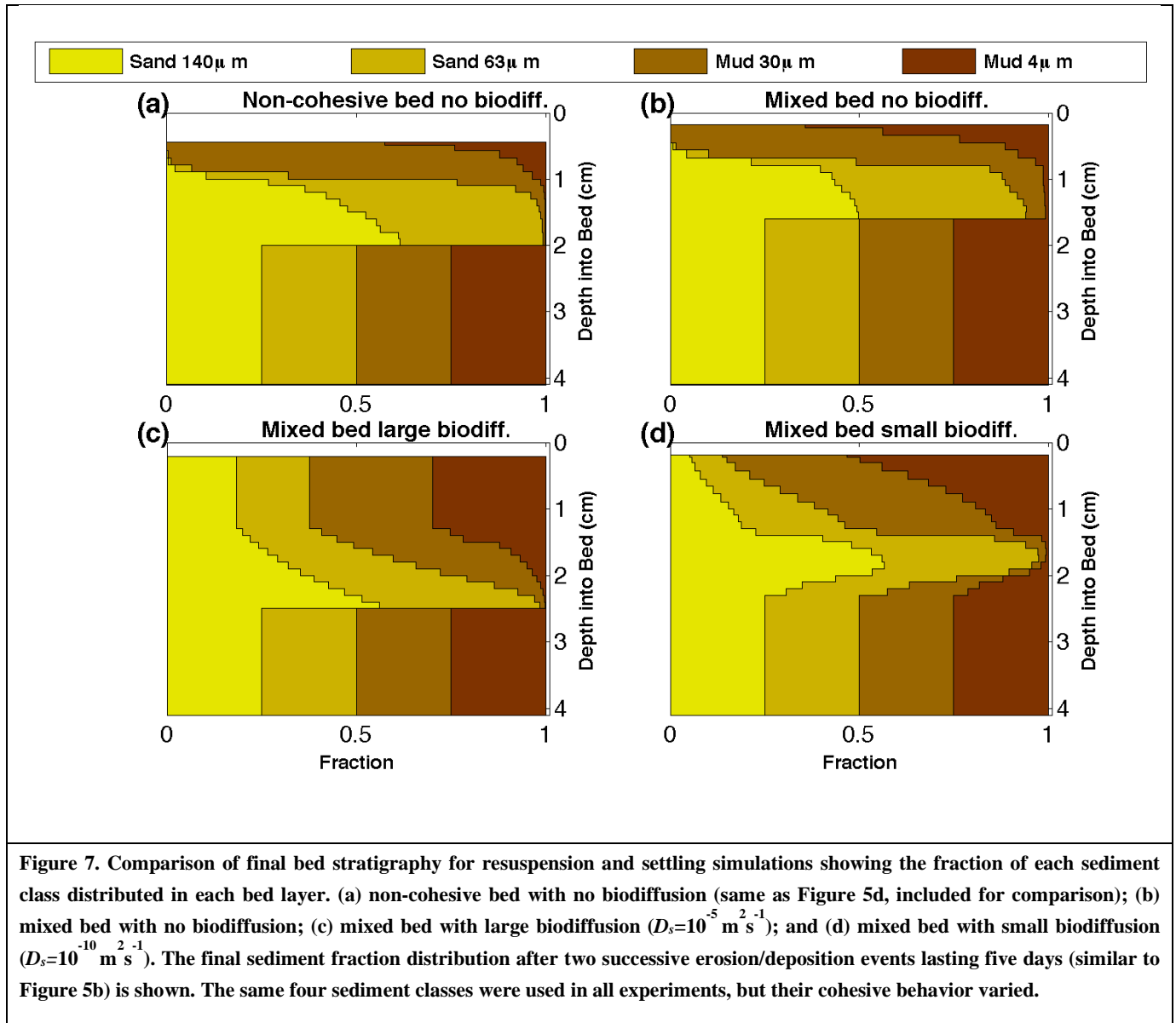


Figure 6. Time series of bottom stress (a) and profiles of critical shear stress for erosion during four distinct conditions: (b) initial bed condition; (c) eroded bed (after 1.3 days with $\tau_b = 1.0$ Pa); (d) after slow but continuous erosion and reduced bulk critical stress profile due to swelling after 30 days more with $\tau_b = 1.0$ Pa); and (e) rapid deposition after a day of low stress with $\tau_b = 0.1$ Pa). In the lower panels, the solid red line is the magnitude of the bottom stress (τ_b), the dashed magenta line is the equilibrium profile of bulk critical stress for erosion $\tau_{cb}(z)$, and the solid purple line is the instantaneous profile of bulk critical stress for erosion. The solid black line is the instantaneous position of the top of the bed at each time, with the initial bed elevation starting at zero.



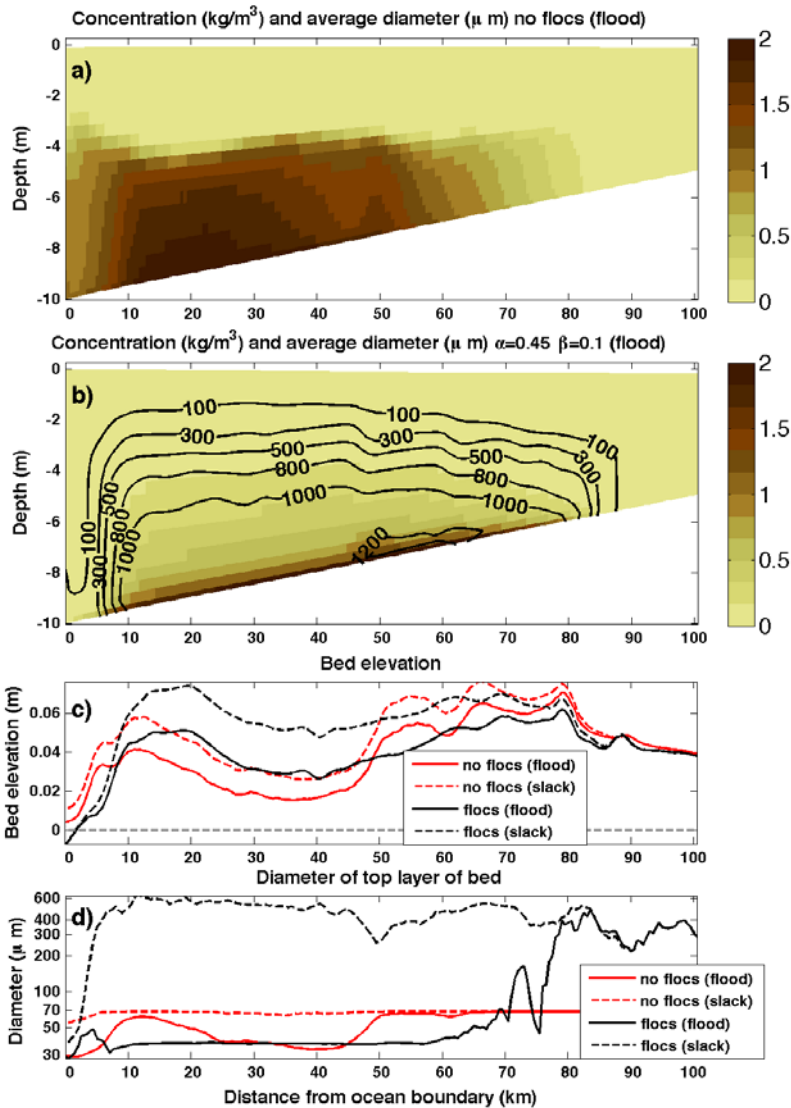


Figure 8. Comparison of estuarine turbidity maxima simulations with and without floc dynamics. a) Two-dimensional (along-estuary and vertical) snapshot of suspended particle concentrations (shaded) without floc dynamics near the end of flood tide. All of the suspended material was in the 37- μm class. b) Snapshot of suspended particle concentrations at the same time in the simulation, but with simulated floc dynamics (shading), overlain by contours of mean particle diameters. c) Along-estuary profiles of bed elevations for simulations without floc dynamics (red) and with floc dynamics (black) at the peak of flood tide (solid lines) and at post-flood slack tide (dashed lines). d) Along-estuary profiles of mean particle diameter in the top layer of the seabed, using the same notation as (c).

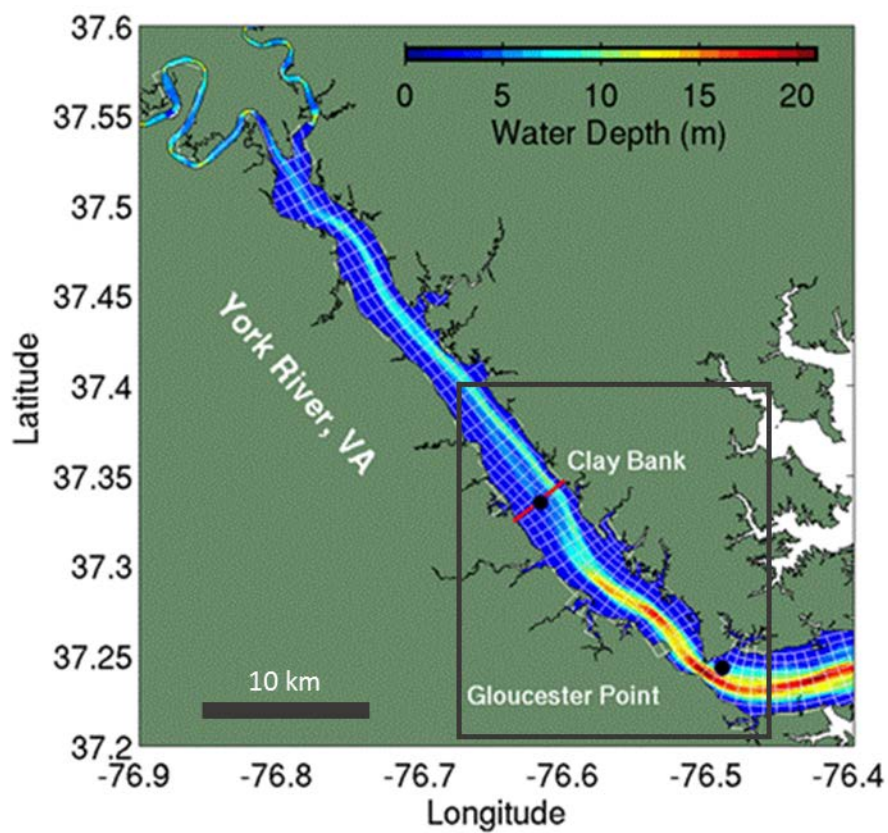


Figure 9. York River bathymetry (color scale), and model grid (white lines show every fifth grid line in the along- and across-channel directions). The region outlined in grey is expanded in Figure 10.

